JGP Journal of General Physiology

COMMUNICATION

Mechanotransduction by Membrane Proteins

TMEM120A/TACAN inhibits mechanically activated PIEZO2 channels

John Smith Del Rosario[1*], Matthew Gabrielle[1*], Yevgen Yudin[1], and Tibor Rohacs[1]

PIEZO2 channels mediate rapidly adapting mechanically activated currents in peripheral sensory neurons of the dorsal root ganglia (DRG), and they are indispensable for light touch and proprioception. Relatively little is known about what other proteins regulate PIEZO2 activity in a cellular context. TMEM120A (TACAN) was proposed to act as a high threshold mechanically activated ion channel in nociceptive DRG neurons. Here, we find that *Tmem120a* coexpression decreased the amplitudes of mechanically activated PIEZO2 currents and increased their threshold of activation. TMEM120A did not inhibit mechanically activated PIEZO1 and TREK1 channels and TMEM120A alone did not result in the appearance of mechanically activated currents above background. *Tmem120a* and *Piezo2* expression in mouse DRG neurons overlapped, and siRNA-mediated knockdown of *Tmem120a* increased the amplitudes of rapidly adapting mechanically activated currents and decreased their thresholds to mechanical activation. Our data identify TMEM120A as a negative modulator of PIEZO2 channel activity, and do not support TMEM120A being a mechanically activated ion channel.

Introduction

PIEZO2 is a nonselective cation channel that is responsible for the rapidly adapting mechanically activated currents in dorsal root ganglia (DRG) neurons (Coste et al., 2010). PIEZO2 plays crucial roles in light touch and proprioception both in mice and in humans (Kefauver et al., 2020). In humans, loss of function mutations in *PIEZO2* lead to impaired proprioception, loss of discriminative touch perception, as well as ataxia and muscular dystrophy (Chesler et al., 2016). In mice, combined deletion of *Piezo2* in DRG neurons and in Merkel cells resulted in a profound loss of light touch (Ranade et al., 2014). Selective deletion of *Piezo2* in proprioceptive neurons in mice recapitulated not only ataxia, but also much of the skeletal abnormalities observed in human loss of function patients (Assaraf et al., 2020).

In contrast to its well-established roles in light touch and proprioception, the role of PIEZO2 channels in detecting painful stimuli is less clear. Genetic deletion of *Piezo2* in DRG neurons and Merkel cells resulted in no change in sensitivity to noxious mechanical stimuli and no change in mechanical allodynia in inflammation (Ranade et al., 2014). Deletion of *Piezo2* in a different subset of DRG neurons, on the other hand, reduced sensitivity to noxious mechanical stimuli, as well as reduced inflammatory and neuropathic mechanical allodynia (Murthy et al., 2018b). In another study, deletion of *Piezo2* in DRG neurons increased threshold to light touch, but paradoxically reduced the threshold to painful mechanical stimuli, indicating that activation of PIEZO2 channels may reduce pain (Zhang et al., 2019), in accordance with the gate control theory of pain (Melzack and Wall, 1965). These data highlight the potentially complex role of PIEZO2 in detecting noxious mechanical stimuli.

PIEZO2 is not the only mechanically activated channel in DRG neurons, and it is not the sole sensor responsible for all aspects of somatosensory touch and mechanical pain (Kefauver et al., 2020). Several novel putative mechanically activated channels have been identified in recent years, including Tentonin3 (TMEM150C; Hong et al., 2016), Elkin1 (TMEM87A; Patkunarajah et al., 2020), OSCAs (TMEM63; Murthy et al., 2018a), and TACAN (TMEM120A; Beaulieu-Laroche et al., 2020). The physiological roles of these novel putative mechanically activated channels are not very well understood.

Tentonin3 (TMEM150C) was proposed to be a component of slowly adapting mechanically activated currents in proprioceptive DRG neurons, and its genetic deletion resulted in abnormal

[1]Department of Pharmacology, Physiology and Neuroscience, Rutgers New Jersey Medical School, Newark, NJ.

*J.S. Del Rosario and M. Gabrielle contributed equally to this paper. Correspondence to Tibor Rohacs: tibor.rohacs@rutgers.edu

J.S. Del Rosario's present address is Washington University Pain Center and Department of Anesthesiology, Washington University School of Medicine, St. Louis, MO.
This work is part of a special issue on mechanotransduction by membrane proteins.

gait and loss of motor coordination (Hong et al., 2016). Later its function as a mechanically activated channel was debated (Dubin et al., 2017; Hong et al., 2017; Parpaite et al., 2021) and it was proposed that Tentonin3 acts as a modulator of PIEZO2, PIEZO1, and TREK1 channel activity (Anderson et al., 2018).

TMEM120A was also proposed to be responsible for the slowly adapting mechanically activated currents in small-to-medium nonpeptidergic nociceptive DRG neurons (Beaulieu-Laroche et al., 2020). Cells transfected with *Tmem120a* displayed currents in response to negative pressure in the cell-attached mode that were above those in control cells, but not when stimulated by indentation with a glass probe in whole-cell patch-clamp experiments (Beaulieu-Laroche et al., 2020). Inducible genetic deletion of *Tmem120a* in nonpeptidergic *Mrgprd* positive DRG neurons in mice resulted in reduced behavioral responses to painful mechanical stimuli. siRNA-mediated knockdown of *Tmem120a* reduced the proportion of ultra-slowly-adapting mechanically activated (MA) currents in *Trpv1* expressing DRG neurons, but it was not tested whether their proportion also decreases in neurons with conditional deletion of *Tmem120a* (Beaulieu-Laroche et al., 2020). *Tmem120a* knockdown in DRG neurons by intrathecal administration of antisense oligodeoxynucleotides in rats reduced mechanical hyperalgesia induced by intradermal administration of various proinflammatory compounds, but had no effect on mechanical hyperalgesia in chemotherapy-induced neuropathic pain (Bonet et al., 2020).

Recently, the cryo-EM structure of TMEM120A was reported by several groups (Niu et al., 2021; Rong et al., 2021; Xue et al., 2021). All three groups found that the protein forms a dimer, and located a coenzyme-A molecule in the structure. The protein showed structural homology to the ELOVL family of lipid modifying enzymes (Nie et al., 2021), indicating that TMEM120A may function as a lipid modifying enzyme. Furthermore, all three publications found that expression of *Tmem120a* did not induce the appearance of mechanically activated currents, in contrast to the findings of Beaulieu-Laroche et al. (2020). A fourth group also determined the structure of TMEM120A, which did not contain coenzyme-A, and they found that expressing a mutant (M207A) of *Tmem120a* resulted in the appearance of small mechanically activated currents evoked by negative pressure in the cell-attached configuration (Chen et al., 2022).

Here, we examined whether TMEM120A can act as a modulator of PIEZO channels. We found that coexpression of *Tmem120a* with *Piezo2* resulted in a robust decrease in the amplitudes of mechanically activated currents and an increase in their mechanical thresholds in whole-cell patch-clamp experiments compared to cells expressing *Piezo2* alone. On the other hand, coexpressing *Tmem120a* with *Piezo1* did not have a significant effect on mechanically induced currents either when the cells were stimulated with a blunt glass probe in the whole-cell configuration, or when negative pressure was used in cell-attached patches. Expressing *Tmem120a* alone did not induce mechanically activated currents above background levels observed in control cells. *Tmem120a* showed broad expression in most DRG neurons, including neurons expressing *Piezo2*. siRNA-mediated knockdown of *Tmem120a* did not decrease the proportion of slowly adapting currents, but it increased the amplitudes and decreased the thresholds of rapidly adapting mechanically activated currents in DRG neurons. Our work identifies TMEM120A as a negative modulator of PIEZO2 channels.

Materials and methods

Cell culture

Human Embryonic Kidney 293 (HEK293) cells were purchased from American Type Culture Collection (ATCC; catalogue number CRL-1573), RRID: CVCL_0045. Cell identity was verified by short tandem repeat analysis at ATCC. Additional cell authentication was not performed, but passage number of the cells was monitored, and cells were used up to passage number 25–30 from purchase, when a new batch of cells was thawed with low passage number. HEK293 cells were cultured in MEM (Gibco) with 10% FBS (Gemini) and 100 IU/ml penicillin plus 100 µg/ml streptomycin (Gemini) in 5% CO_2 at 37°C.

Piezo1 deficient Neuro2A (N2A) cells, in which endogenous *Piezo1* was deleted by CRISPR (Moroni et al., 2018; Romero et al., 2020), were cultured in Dulbecco's Modified Eagle Medium (Gibco), 1% penicillin–streptomycin, and 10% FBS.

HEK293 cells were transfected with Effectene reagent (Qiagen) in 35-mm tissue culture dishes with 200 ng *Piezo1* or *Piezo2* and 200 ng *Tmem120a* or 50 ng tdTomato. N2A-Pz1-KO cells used for patch-clamp experiments in the whole-cell configuration were transfected using the same reagent with 500 ng *Piezo2* and 500 ng *Tmem120a*-tdTomato or 125 ng tdTomato. N2A-Pz1-KO cells used for experiments in the cell-attached configuration were transfected with 1,500 ng *Piezo1* or 1,500 ng TREK1 and 1,500 ng *Tmem120a*-Tom or 375 ng tdTomato (listed concentrations of *Tmem120a*-tdTomato and tdTomato cDNA were used for experiments when transfected by themselves). The day after transfection, the cells were split and plated on poly-Lysine–coated 12-mm glass cover slips for patch-clamp experiments, which were performed 48–72 h after transfection.

DRG neurons

DRG neurons were isolated as described previously (Borbiro et al., 2015; Del Rosario et al., 2020). All animal procedures were approved by the Institutional Animal Care and Use Committee at Rutgers New Jersey Medical School. Mice were kept in a barrier facility under a 12/12-h light/dark cycle. Wild-type C57BL6 mice (2–4 mo old) from either sex (The Jackson Laboratory) were anesthetized with i.p. injection of ketamine (100 mg/kg) and xylazine (10 mg/kg) and perfused via the left ventricle with ice-cold Hank's buffered salt solution (HBSS; Life Technologies). DRGs were harvested from all spinal segments after laminectomy and removal of the spinal column and maintained in ice-cold HBSS for the duration of the isolation. Isolated ganglia were cleaned from excess nerve tissue and incubated with type 1 collagenase (2 mg/ml; Worthington) and dispase (5 mg/ml; Sigma-Aldrich) in HBSS at 37°C for 30 min, followed by mechanical trituration. Digestive enzymes were then removed after centrifugation of the cells at 100 *g* for 5 min.

Isolated DRG neurons were resuspended in Nucleofector Solution (Mouse Neuron Nucleofactor Kit, VPG-1001; Lonza) and predesigned fluorescently labelled siRNA directly against mouse *Tmem120a* from Qiagen-FlexiTube (cat. S101311919) or AllStars Neg. siRNA (cat. 1027294) was added at a final concentration of 300 nM. The transfection reactions were transferred to aluminum cuvettes for Nucleofection via Nucleofector 2b device (Lonza). After Nucleofection, DRG neurons were seeded onto laminin-coated glass coverslips and cultured in serum containing Dulbecco's Modified Eagle Medium, and fresh medium was added every 24 h. Whole-cell patch-clamp experiments were performed 48–72 h after transfection using neurons displaying siRNA-mediated fluorescence.

Whole-cell patch clamp

Whole-cell patch-clamp recordings were performed at room temperature (22–24°C) as described previously (Borbiro et al., 2015). Briefly, patch pipettes were prepared from borosilicate glass capillaries (Sutter Instrument) using a P-97 pipette puller (Sutter instrument) and had a resistance of 2–7 MΩ. After forming gigaohm-resistance seals, the whole-cell configuration was established, and the MA currents were measured at a holding voltage of −60 mV using an Axopatch 200B amplifier (Molecular Devices) and pClamp 10. Currents were filtered at 2 kHz using low-pass Bessel filter of the amplifier and digitized using a Digidata 1,440 unit (Molecular Devices). All measurements were performed with extracellular solution containing 137 mM NaCl, 5 mM KCl, 1 mM $MgCl_2$, 2 mM $CaCl_2$, 10 mM HEPES, and 10 mM glucose (pH adjusted to 7.4 with NaOH). The patch pipette solution contained 140 mM K^+ gluconate, 1 mM $MgCl_2$, 2 mM Na_2ATP, 5 mM EGTA, and 10 mM HEPES (pH adjusted to 7.2 with KOH).

Mechanically activated currents were measured from isolated DRG neurons, transiently transfected HEK293 cells, and transiently transfected *Piezo1* deficient N2A cells, as previously described (Borbiro et al., 2015). Briefly, mechanical stimulation was performed using a heat-polished glass pipette (tip diameter, about 3 µm), controlled by a piezoelectric crystal drive (Physik Instrumente) positioned at 60°C to the surface of the cover glass. The probe was positioned so that 10-µm movement did not visibly contact the cell but an 11.5-µm stimulus produced an observable membrane deflection. Measurements from cells that showed significant swelling after repetitive mechanical stimulation or had substantially increased leak current were discarded. The inactivation kinetics from MA currents were measured by fitting the MA current with an exponential decay function in the Clampfit software, which measured the inactivation time constant (tau). We used the currents evoked by the third stimulation after the threshold in most experiments, except in cells where only the two largest stimuli evoked a current, where we used the current evoked by the largest stimulus, provided it reached 40 pA.

For the DRG neuron experiments, to categorize mechanically activated currents as rapidly, intermediate, and slowly adapting, we used the criteria from our previous publications (Borbiro et al., 2015; Del Rosario et al., 2020). We considered currents to be rapidly adapting if they fully inactivated before end of the 200-ms mechanical stimulus. The inactivation time constants (tau) of these currents were 14.80 ± 3.17 ms (mean ± SD, range 8–22 ms), similar to that in our earlier work (Borbiro et al., 2015; Del Rosario et al., 2020). This inactivation time constant was very similar to those in HEK293 or *Piezo1* deficient N2A cells transfected with *Piezo2* (Fig. S1, F, L, and R), indicating that these currents were predominantly mediated by PIEZO2. Note that these inactivation time constants are longer than the originally reported <10 ms for PIEZO2 (Coste et al., 2010), but the inactivation time constants of both PIEZO1 and PIEZO2 show considerable variability between different research laboratories (Szczot et al., 2017; Wu et al., 2017; Romero et al., 2019).

Intermediate adapting currents did not fully inactivate, but the leftover current at the end of the mechanical simulation was <50% of the peak current. The inactivation time constant for these currents was 36.35 ± 12.4 ms (range 22–55 ms). Slow adapting currents also did not fully inactivate, and the leftover current at the end of the mechanical simulation was >50% of the peak current, and/or the time constant was over 55 ms. The inactivation time constant for these currents was 88.14 ± 34.14 (range 58–151 ms).

Cell-attached patch clamp

Patch-clamp recordings in the cell-attached configuration were performed at room temperature (22–24°C) similar to that described previously (Lewis and Grandl, 2015). After forming gigaohm-resistance seals, MA currents were measured at a holding voltage of −80 mV for PIEZO1 currents and at 0 mV for TREK1 currents, using an Axopatch 200B amplifier (Molecular Devices) and pClamp 10. Currents were filtered at 2 kHz using low-pass Bessel filter of the amplifier and digitized using a Digidata 1,440 unit (Molecular Devices). Mechanical stimulation in cell-attached patches was performed using a high-speed pressure clamp (Besch et al., 2002; HSPC-1, ALA Scientific) controlled by pClamp 11.1 software (Molecular Devices), as described earlier (Borbiro et al., 2015).

All measurements were performed with a bath solution containing, 140 mM KCl, 1 mM $MgCl_2$, 10 mM HEPES, and 10 mM glucose (pH adjusted to 7.4 with KOH) to bring the membrane potential of the cells close to zero. The patch pipette solution contained 130 mM NaCl, 5 mM KCl, 1 mM $MgCl_2$, 1 mM $CaCl_2$, 10 mM HEPES, and 10 mM TEA-Cl (pH adjusted to 7.4 with NaOH).

TIRF microscopy

HEK293 cells were transiently transfected with cDNA encoding *Tmem120a*-tdTomato, or tdTomato, and GFP-*Piezo1* or GFP-*Piezo2*. The next day, the transfected cells were plated on poly-L-lysine–coated 35-mm round coverslip (#1.5 thickness; Thermo Fisher Scientific). The cells were used for TIRF imaging 2 d after transfection. Cells plated on the coverslip were placed into a recording chamber filled with extracellular solution containing (in mM) 137 NaCl, 5 KCl, 1 $MgCl_2$, 10 HEPES, and 10 glucose (pH 7.4). TIRF images were obtained at room temperature using a Nikon Eclipse Ti2 microscope. Fluorescence excitation was performed using a 15-mW solid state 488- and 561-nm laser at

90% of the maximal power through a CFI Apochromat TIRF 60X oil objective (NA of 1.49). Images were captured using an ORCA-Fusion Digital CMOS camera (Hamamatsu) through emission filters 525/50 and 600/50 nm for the green and red channel, respectively.

To visualize actin and tubulin cytoskeleton, the cells were labeled with either Sir-Actin (CY-SC001) or Spy650-tubulin (CY-SC503; Cytoskeleton, Inc.) according to the manufacturer's instructions. Live cells were incubated for 1 h at 37°C with either Sir-Actin (2 µM) or Spy650-tubulin (500× dilution of the stock solution recommended by the manufacturer). The cells were washed with the extracellular solution before imaging to remove the excess dyes. For cytoskeletal disruption, cells were incubated in either 10 µM colchicine (C-9754; Millipore Sigma) for 1 h or 1 µM cytochalasin D (11330; Cayman Chemicals) for 24 h. To visualize the probes, the cells were illuminated by the 640-nm 15 mW solid state laser, and emission was collected using a 700/75-nm emission filter.

The images were analyzed using Nikon NIS-Elements AR Analysis software. Regions of interest (ROIs) were generated by hand drawing the outline of individual cells allowing for analysis over the total area of each cell in the TIRF angle. Mean fluorescence intensities within these single-cell ROIs were determined via Nikon NIS-Elements AR Analysis software. To correct for background fluorescent signal, a single rectangular ROI was generated on each image over an area absent of any cell or cell debris, and mean fluorescent intensity was calculated. Background mean intensity was averaged from each image per coverslip and subtracted from the mean intensity of the single-cell ROIs. The mean fluorescent intensities from each cell on a single coverslip were averaged (5–22 total cells/coverslip) and plotted. To determine colocalization, the same single-cell ROIs were used. NIS-Elements AR Analysis software generated Pearson's correlation coefficients between designated fluorescent channels as a measure of colocalization. The Pearson's correlation coefficients from each cell on a single coverslip was averaged and plotted. GFP-PIEZO2 and GFP-PIEZO1 fluorescent puncta were identified using the "Spot Detector" feature of NIS-Elements AR Analysis software for each cell. The number of puncta detected was normalized by their respective cell's area. Values from each cell on individual coverslips were averaged and plotted.

Confocal microscopy

Measurements were conducted with an Olympus FluoView-1000 confocal microscope in the frame scan mode using a 60X water immersion objective at room temperature. Green fluorescence was measured using excitation wavelength of 473 nm; emission was detected through a 515/50-nm band-pass filter. Red fluorescence was measured using excitation wavelength of 559 nm; emission was detected through a 585/50-nm band-pass filter. Image analysis was performed using Olympus FluoView-1000 and ImageJ.

Western blotting

Piezo1 deficient N2A cells (10^6) were transfected with siRNA against mouse *Tmem120a* from Qiagen-FlexiTube (cat. S101311919) or AllStars Neg. siRNA (cat. 1027294) at a final concentration of 300 nM. Nucleofection was used as previously described. The cells were plated on 35-mm tissue culture dishes and harvested 48 h after transfection via scraping in Cell-Lytic-M lysis buffer (Cat. No.: C2978; MilliporeSigma) containing Halt Protease Inhibitor Cocktail (Cat. No.: 78438; Thermo Fisher Scientific). Protein samples were denatured in Laemmli sample buffer (Cat. No.: 161-0747; BioRad) and 2-mercaptoethanol for 1 h in a 37°C water bath. Samples were run on BioRad 4–15% mini-protean gels (Cat. No.: 4561084). Semidry transfers were performed using BioRad Trans-blot Turbo Transfer System onto nitrocellulose membranes (Cat. No.: 1704158; BioRad). The membranes were blocked for 1 h at room temperature in Tris-buffered saline with 0.1% Tween-20 (TBS-T) with 5% milk and incubated with 1:500 rabbit anti-TMEM120A antibodies (Cat. No.: MBS3223965; MyBioSource) in TBS-T with 5% milk overnight at 4°C. The membranes were probed with 1:10,000 goat anti-rabbit HRP antibodies (Cat. No.: G21234; Invitrogen) in TBS-T with 5% milk for 1 h at room temperature. Super Signal West Femto Max Sensitivity substrate (Cat. No.: 34095; Thermo Fisher Scientific) was used to develop the membranes and they were imaged with a FlourChem-8800 imager. The membranes were stripped using Restore Stripping buffer (Cat. No.: 46430; Thermo Fisher Scientific) then reblocked and probed with 1:5,000 rabbit anti-βTubulin antibodies (Cat. No.: NB600-936; Novus) in TBS-T with 5% milk overnight at 4°C. The membranes were developed and imaged as previously described. Images were analyzed using ImageJ.

RNAScope in situ hybridization

DRG isolation was performed as described before with transcardial perfusion under deep anesthesia first with 10 ml of HBSS and after with 10 ml of 4% formaldehyde. L3–L5 DRGs were collected from mice; the tissues were postfixed for 1 h in 4% formaldehyde and dehydrated in a series of gradient sucrose concentration (10, 20, and 30%). After freezing in O.C.T. compound block (Sakura Finetech), DRGs were sectioned into 12-µm-thick slices, and RNAScope assay was then carried out as previously described (Su et al., 2020).

Simultaneous detection of mouse RNA transcripts for *Piezo2*, *Tmem120a*, and various neuronal markers was performed on fixed, frozen DRG sections using Advanced Cell Diagnostics (ACD) RNAScope Multiplex Fluorescent Reagent Kit v2 (cat number: 323110) according to the manufacturer's instructions, and commercially available probes for Mm-*Tmem120a* (cat number: 513211), Mm-*Piezo2* (cat number: 400191-C2), Mm-*Trpv1* (cat number: 313331-C3), Mm-*Th* (cat number: 317621-C3), Mm-*Nefh* (cat number: 443671-C3), and *Calcb* (CGRP2; cat number: 425511-C3) were purchased from ACD.

In short, the sections were postfixed in prechilled 4% paraformaldehyde in PBS for 15 min at 4°C, washed three times with PBS for 5 min each before dehydration through 50, 70, and 100 and 100% ethanol for 5 min each. We then treated slides with a protease 4 for 20 min and washed in distilled water. Probe hybridization and signal amplification were performed according to manufacturer's instructions. The following fluorophores were used to detect corresponding RNAScope probes: Opal 520, 570,

and 690 reagent kits (Akoya Biosciences). Cells were stained with DAPI (ACD) and mounted on the slide with Gold Antifade Mountant. Slides were imaged on a Nikon A1R confocal microscope with a 20× Plan Apo air objective, NA 0.75; and images were quantified in Nikon NIS-Elements.

Totally, three mice were used in the experiment, from each animal were harvested 6 L3–5 DRG ganglions; after sectioning of the tissue, six slices from each animal were treated, and two to three slices from each animal were randomly selected for analysis. A total number of 2,075 neurons for the *Trpv1* probe, 1,863 neurons for the *Th* probe, 1,821 neurons for *Nefh*, and 1,839 neurons for the *Calcb* probe were analyzed.

Neuronal cell borders were determined and segmented manually dependently on the level of the fluorescent probes signal and DIC images. Cells were considered as signal positive if the mean fluorescence signal in the ROI exceeded 0.5 times the SD of the fluorescence signal in this channel.

cDNA constructs

The *Piezo1*-IRES-GFP and the *Piezo2* pcDNA clones were from Dr. Ardem Patapoutian, Scripps Research, San Diego, CA (Coste et al., 2010). The following cDNA clones were purchased from Origene: myc-tagged mouse *Tmem120A* (MR205146, NM_172541), myc-tagged mouse *Tmem120b* (MR205067, NM_001039723), and myc-tagged mouse *Trek1* (KCNK2; MR206535, BC062094). The GFP-tagged *Piezo1* construct (GFP-*Piezo1*) was generated by subcloning the mouse *Piezo1* to the pcDNA3.1(-) vector from the original IRES-GFP vector then PCR cloning GFP and ligating it to the N-terminus of Piezo1 (Jiang et al., 2021). The GFP-tagged *Piezo2* construct (GFP-*Piezo2*) was generated by PCR cloning GFP and ligating it to the N-terminus of Piezo2 in the pCMV SPORT6 vector. The tdTomato-tagged *Tmem120a* construct was generated by PCR cloning *Tmem120a* using the Origene MR205146 clone as a template and subcloning it to the ptdTomato-N1 vector (Clontech), placing the tdTomato tag to the C-terminus of *Tmem120a*. For PCR cloning, the Pfu-Ultra proofreading enzyme (Agilent) was used and the constructs were verified with sequencing.

Statistics

Data are represented as mean ± SEM plus scatter plots. For normally distributed data, statistical significance was calculated either with two sample *t* test (two tailed), or ANOVA, with Bonferroni post hoc test. Normality was assessed by the Shapiro Wilk test or the Lilliefors test. For non-normally distributed data, Wilcoxon or Mann-Whitney tests were used as appropriate. Variance was assessed using Levene's test for homogeneity of variance (centered on median). For normally distributed data with unequal variance, Welch's *t* tests were used as appropriate. The specific tests for each experiment are described in the figure legends. No statistical method was used to predetermine sample sizes, but our sample sizes are similar to those generally employed by the field. Experiments were performed in a random order. Most statistical calculations and data plotting were performed using the Origin 2021 software.

Online supplemental material

Fig. S1 shows additional data analysis and plots from the data shown in Fig. 1, and data indicating that TMEM120B does not inhibit Piezo2 currents. Fig. S2 shows additional data analysis and plots from the data shown in Fig. 2. Fig. S3 shows surface expression data with TIRF, Fig. S4 shows representative confocal images for the cellular localization of TMEM120A, Figs. S5 and S6 show TIRF images with cytoskeletal probes for actin and tubulin, and Fig. S7 shows additional analysis and supporting data for Fig. 4.

Results

We first transiently transfected HEK293 cells with *Piezo2* and *Tmem120a*, and measured mechanically activated currents in response to indentation of the cell membrane with a blunt glass probe in whole-cell patch-clamp experiments. Cells expressing *Piezo2* alone displayed rapidly adapting mechanically activated currents that showed increased amplitudes in response to deeper indentations (Fig. 1, A–C). When *Tmem120a* was co-transfected with *Piezo2*, the majority of the cells did not show responses to mechanical indentations, with a small number of cells responding to stronger stimuli, resulting in significantly decreased average current amplitudes (Fig. 1, A–C).

To ensure that all cells we patched indeed expressed *Tmem120a* and *Piezo2*, we transfected HEK293 cells with *Tmem120a* tagged with tdTomato, and *Piezo2* tagged with GFP, and patched cells displaying both red and green fluorescence. Coexpression of *Tmem120a*-tdTomato robustly decreased GFP-PIEZO2 current amplitudes (Fig. 1, D–F) indicating that the responses in the *Tmem120a* transfected group were unlikely to be due to the lack of TMEM120A, and the lack of responses were not due to the lack of PIEZO2. The thresholds for mechanical activation among the responding cells were significantly higher in HEK cells transfected with *Tmem120a* compared to control cells (Fig. S1, E and K).

To ensure that the reduction in PIEZO2 channel activity is not specific to HEK293 cells, we also coexpressed *Tmem120a* with *Piezo2* in N2A cells in which *Piezo1* was deleted with CRISPR (Moroni et al., 2018; Romero et al., 2020). In these cells, we could perform deeper indentations of the cell without losing the seal, thus we detected larger currents. Similar to HEK293 cells, co-expression of *Tmem120a*-tdTomato with GFP-*Piezo2* strongly reduced mechanically activated currents (Fig. 1, G–I).

Both in HEK293 cells and in N2A cells, we stimulated all cells with increasing indentations until the seal was lost, but we only plotted data in Fig. 1 up to the indentation depth where all cells still had intact seals. Fig. S1 displays the full data that includes cells that responded at higher indentation depths, and representative traces for mechanically activated currents in *Tmem120a* expressing cells at higher indentation levels. The overall responsiveness of control cells was 94–100%, while the *Tmem120a* expressing cells was 33–54% (Fig. S1, A, B, G, H, M, and N). The peak current amplitudes regardless of the indentation depth, i.e., just before the seal was lost, were also significantly lower in *Tmem120a* expressing cells in all three groups (Fig. S1, D, J, and P).

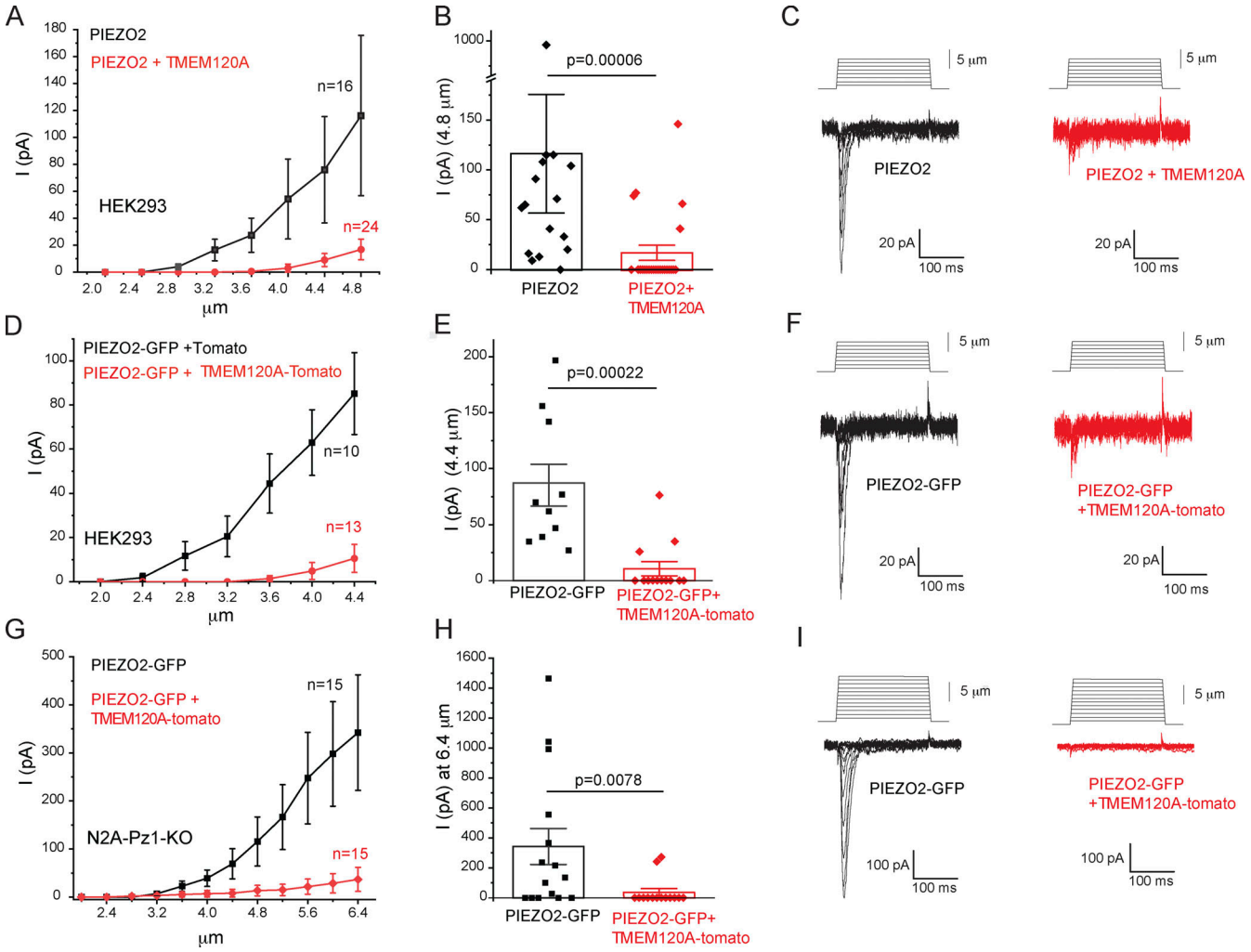

Figure 1. **TMEM120A inhibits PIEZO2 currents.** Whole-cell patch-clamp experiments at −60 mV in cells transiently transfected with *Piezo2* with or without *Tmem120a* were performed as described in the Materials and methods section. **(A)** HEK293 cells were transfected with *Piezo2* and GFP with or without *Tmem120a*. In some cells, GFP-tagged *Piezo2* was used instead of *Piezo2* plus GFP. Current amplitudes are plotted (mean ± SEM) for *Piezo2* expressing cells (black) and for cells expressing *Piezo2* and *Tmem120a* (red). **(B)** Scatter plots and mean ± SEM for current amplitudes at 4.8 µm indentation. Statistical significance was calculated with the Mann-Whitney test. **(C)** Representative current traces. **(D)** HEK293 cells were transfected with GFP-tagged *Piezo2* and with tdTomato-tagged *Tmem120a* or tdTomato. Current amplitudes are plotted (mean ± SEM) for *Piezo2* expressing cells (black) and for cells expressing *Piezo2* and *Tmem120a* (red). **(E)** Scatter plots and mean ± SEM for current amplitudes at 4.4 µm indentation. Statistical significance was calculated with the Mann-Whitney test. **(F)** Representative current traces. **(G)** Piezo1 deficient N2A cells were transfected with GFP-tagged *Piezo2* and with tdTomato-tagged *Tmem120a* or tdTomato. Current amplitudes (mean ± SEM) are plotted for *Piezo2* expressing cells (black) and for cells expressing *Piezo2* and *Tmem120a* (red). **(H)** Scatter plots and mean ± SEM for current amplitudes at 6.4 µm indentation. Statistical significance was calculated with the Mann-Whitney test. **(I)** Representative current traces.

PIEZO2 currents in cells expressing either GFP-*Piezo2* or with tomato-tagged *Tmem120a* showed similar inactivation kinetics in both HEK293 cells and in N2A cells (Fig. S1, L and R). In HEK293 cells, cotransfected with *Piezo2* and nontagged *Tmem120a*, the time constant of inactivation increased slightly but significantly (Fig. S1 F).

We also tested if TMEM120A's close homologue TMEM120B had any effect on PIEZO2 current amplitudes. TMEM120B shares 69% sequence identity with TMEM120A, and the two proteins have a very similar homodimeric structure with six transmembrane helices in each monomer (Ke et al., 2021). Fig. S1, S and T, shows that PIEZO2 current amplitudes were similar in HEK293 cells transfected with, or without *Tmem120b*.

We also patched HEK293 cells expressing *Tmem120a*-tdTomato alone, and we did not observe any mechanically activated currents in response to indentation with a blunt glass probe up to 9.2 µm (data not shown, $n = 11$), in accordance with the original report describing TMEM120A/TACAN (Beaulieu-Laroche et al., 2020).

Next, we tested if TMEM120A modulates the closely related PIEZO1 channels. Coexpression of *Tmem120a* in HEK293 cells did not inhibit PIEZO1 channel activity evoked by indentation with a blunt glass probe in whole-cell patch-clamp experiments (Fig. 2, A–C; and Fig. S2, A and B). Coexpressing *Tmem120b* also did not affect PIEZO1 activity in the whole-cell patch-clamp mode (data not shown).

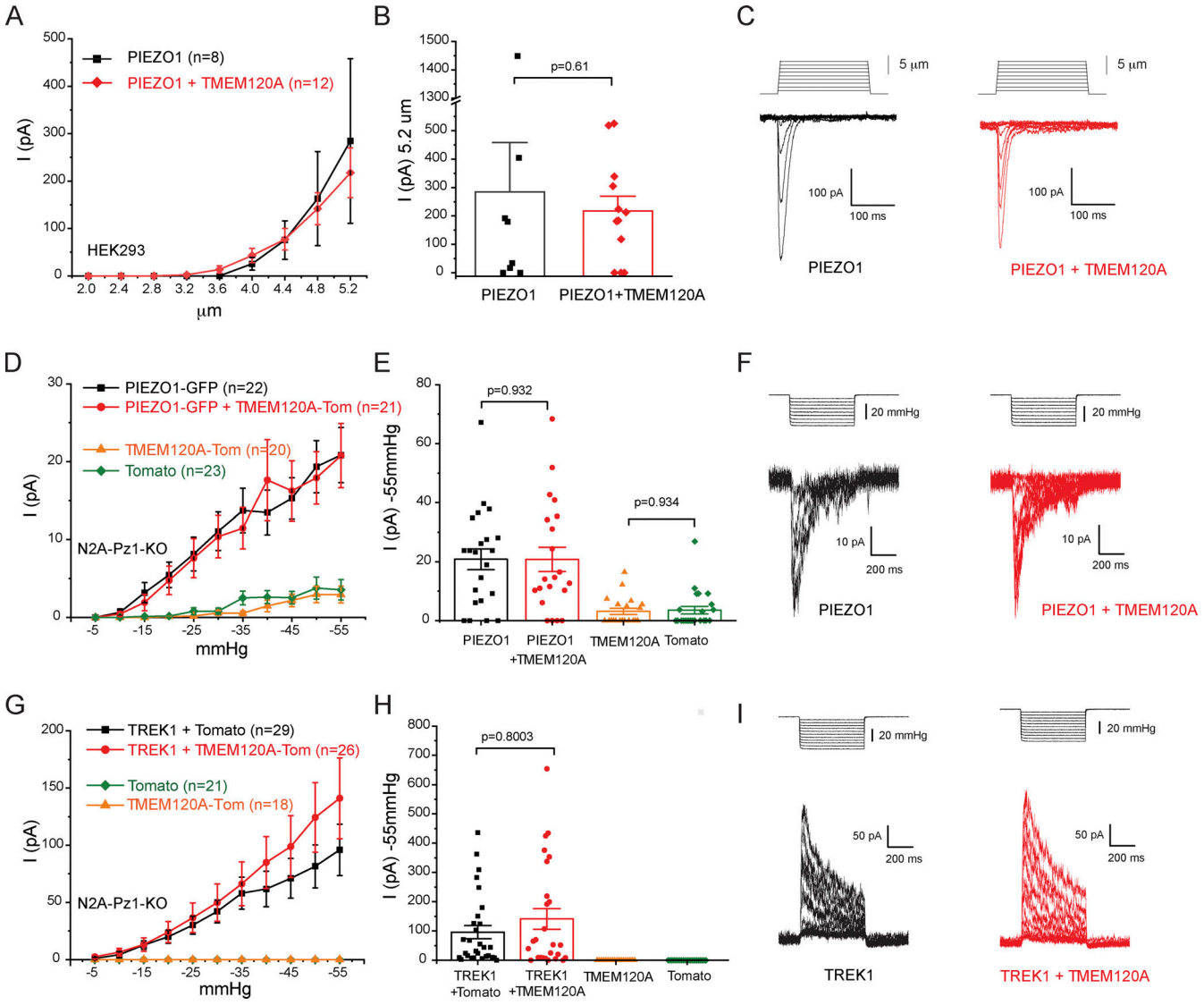

Figure 2. **TMEM120A does not inhibit PIEZO1 and TREK1 currents. (A)** HEK293 cells were transfected with *Piezo1* in IRES-GFP vector, with or without *Tmem120a*. Mechanically activated currents were evoked by increasing indentations with a blunt glass probe in whole-cell patch-clamp experiments. Current amplitudes are plotted (mean ± SEM) for *Piezo1* expressing cells (black) and for cells expressing *Piezo1* and *Tmem120a* (red). **(B)** Scatter plots and mean ± SEM for current amplitudes at 5.2 μm indentation. Statistical significance was calculated with the Mann-Whitney test. **(C)** Representative current traces. **(D)** *Piezo1* deficient N2A cells were transfected with GFP-*Piezo1* with or without *Tmem120a*-tdTomato, and with tdTomato-*Tmem120a* alone or tdTomato alone. Mechanically activated currents were evoked by applying increasing negative pressures through the patch pipette in cell-attached patch-clamp experiments. Measurements were performed at −80 mV holding potential. Current amplitudes are plotted (mean ± SEM) for cells expressing *Piezo1* (black), *Piezo1* and *Tmem120a* (red), *Tmem120a* alone (orange), and tdTomato alone (green). **(E)** Scatter plots and mean ± SEM for current amplitudes at −55 mmHg. Statistical significance was calculated with the Mann-Whitney test. **(F)** Representative current traces. **(G)** *Piezo1* deficient Neuro2A cells were transfected with TREK1 with, or without *Tmem120a*-tdTomato, and with *Tmem120a*-tdTomato alone or tdTomato alone. Mechanically activated currents were evoked by applying increasing negative pressures through the patch pipette in cell-attached patch-clamp experiments. Measurements were performed at 0 mV holding potential. Current amplitudes are plotted (mean ± SEM) for cells expressing TREK1 (black), TREK1 and *Tmem120a* (red), *Tmem120a* alone (orange), and tdTomato alone (green). **(H)** Scatter plots and mean ± SEM for current amplitudes at −55 mmHg. Statistical significance was calculated with the Mann-Whitney test. **(I)** Representative current traces.

Unlike PIEZO2 (Shin et al., 2019), PIEZO1 currents can be reliably evoked by negative pressure in the cell-attached mode (Coste et al., 2010). To test the effect of TMEM120A in this modality, we expressed GFP-*Piezo1* with *Tmem120a*-tdTomato or tdTomato in *Piezo1* deficient Neuro2A cells. Negative pressures applied through the patch pipette reproducibly evoked mechanically activated currents. Current amplitudes in the *Tmem120a* expressing cells were similar to those without *Tmem120a* (Fig. 2, D–F). We also performed experiments in cells only expressing *Tmem120a*, or tdTomato. In contrast to *Piezo1* expressing cells, both groups displayed no or negligible currents at low pressures. Increasing negative pressures evoked small currents in both *Tmem120a*-tdTomato and in tdTomato transfected cells, but the amplitudes of those were

very similar in the two groups (Fig. 2, D and E; and Fig. S2, E–H).

We also tested if TMEM120A had any effect on the activity of TREK1, a mechanically activated K^+ selective ion channel. We evoked outward TREK1 currents in cell-attached patches in *Piezo1* deficient N2A cells by negative pressures at 0 mV (Fig. 2, G–I). Currents in cells cotransfected with tdTomato-*Tmem120a* and TREK1 showed similar current amplitudes to those transfected with TREK1 and tdTomato (Fig. 2, G–I; and Fig. S2, I and J). In cells expressing *Tmem120a*-tdTomato, or tdTomato alone, negative pressures did not induce any currents in these conditions (Fig. 2, G and H; and Fig. S2, K and L).

Next, we performed dual color TIRF imaging to assess cell-surface expression and colocalization of PIEZO2, PIEZO1, and TMEM120A. In TIRF imaging, the intensity of the excitation light decreases exponentially with the distance from the cover glass, only illuminating a narrow layer at the bottom of the cell, representing the plasma membrane and a narrow subplasma membrane region, up to 200 nm (Fish, 2009; Martin-Fernandez et al., 2013; Yamamura et al., 2015). We cotransfected HEK293 cells with GFP-*Piezo1* or GFP-*Piezo2*, and *Tmem120a*-tdTomato or tdTomato. Fig. S3, A and B, shows that TIRF intensity of GFP-PIEZO2 was similar in cells cotransfected with *Tmem120a*-tdTomato or tdTomato. Fig. S3, E and F, shows that coexpression of *Tmem120a*-tdTomato did not change fluorescence intensity of GFP-PIEZO1 either. These data suggest that coexpression of *Tmem120a* did not change the cell-surface expression of PIEZO2 or PIEZO1.

Both GFP-PIEZO2 and GFP-PIEZO1 showed punctate localization in the TIRF images (Fig. S3, A and E), in accordance with earlier reports (Gottlieb and Sachs, 2012; Ellefsen et al., 2019; Ridone et al., 2020; Jiang et al., 2021). The number of GFP-PIEZO2 and GFP-PIEZO1 puncta per area was not different in *Tmem120a* transfected and control cells (Fig. S3, C and G). TMEM120A-tdTomato also showed inhomogeneous distribution and displayed very weak colocalization with PIEZO2 and PIEZO1 with Person's coefficients of ∼0.55. tdTomato alone showed a more homogenous distribution in TIRF images, and its Pearson's coefficient with PIEZO2 and PIEZO1 was only slightly, and not statistically significantly lower than that for TMEM120A-tdTomato (Fig. S3, D and H).

TMEM120A was shown earlier to be present in the plasma membrane using cell-surface biotinylation (Beaulieu-Laroche et al., 2020; Chen et al., 2022), but it was also shown to be localized to the endoplasmic reticulum (Li et al., 2021 *Preprint*) and the nuclear envelope (Batrakou et al., 2015). Consistent with these earlier data, TMEM120A-tdTomato showed not only plasma membrane, but also substantial intracellular localization in confocal microscopy experiments (Fig. S4 A). GFP-PIEZO2 as well as GFP-PIEZO1 also showed substantial localization to intracellular membranes (Fig. S4, B and C), most likely reflecting trafficking to the plasma membrane.

PIEZO2 has been shown to be modulated by both the actin cytoskeleton and microtubules (Jia et al., 2016; Chang and Gu, 2020). To test if TMEM120A acts via altering the organization of the plasma membrane associated cytoskeleton, we labeled HEK293 cells expressing *Tmem120a*-tdTomato and GFP-*Piezo1* or GFP-*Piezo2* with the cell permeable live cell dyes Sir-Actin and Spy650-tubulin and performed TIRF microscopy. Both actin (Fig. S5) and tubulin (Fig. S6) showed a very weak colocalization with PIEZO2 and PIEZO1 (Pearson's coefficients between 0.1–0.4), and TMEM120A did not change this colocalization. TMEM120A also did not change the intensity of actin or tubulin labeling. As positive controls, we treated cells with the actin disrupting agent cytochalasin D, and with the microtubule disrupting colchicine. Cytochalasin D reduced the intensity of actin labeling (Fig. S5, G and H) and colchicine dramatically reduced the intensity of tubulin labeling (Fig. S6, G and H). These data indicate that TMEM120A does not act via altering the cytoskeletal elements adjacent to the plasma membrane.

Next, we tested if *Tmem120a* is expressed in the same neurons as *Piezo2* using RNAScope fluorescence in situ hybridization. We performed triple labeling experiments with probes for *Piezo2*, *Tmem120a* and one of the following neuronal markers: Neurofilament heavy chain (*Nefh*), Tyrosine hydroxylase (*Th*), Transient receptor potential vanilloid 1 (*Trpv1*), and calcitonin gene-related peptide 2 (*Calcb*; Fig. 3). *Nefh* labels neurons corresponding to myelinated Aβ and Aδ fibers and proprioceptors, *Th* labels a subset of nonpeptidergic C fiber low-threshold mechanoreceptors, *Trpv1* noxious heat-sensitive C-fiber nociceptors, while *Calcb* small peptidergic C-fibers, and Aδ fiber nociceptors, with some expression in a subset of nonpeptidergic high-threshold mechanoreceptors (Le Pichon and Chesler, 2014; Usoskin et al., 2015). *Tmem120a* was expressed in >90% of neurons. *Piezo2* was found in 60–70% of neurons and >95% of the *Piezo2* positive neurons also expressed *Tmem120a*. *Piezo2* showed a variable level of coexpression with the different neuronal markers (Fig. 3, B, E, H, and K), the highest being *Th* (Fig. 3 E), consistent with earlier work showing high Piezo2 levels in these neurons (Usoskin et al., 2015) and these neurons being low-threshold mechanoreceptors (Le Pichon and Chesler, 2014). *Piezo2* showed the lowest coexpression with *Trpv1*, which is consistent with low responsiveness of TRPV1 positive cells to mechanical stimuli (Borbiro et al., 2015).

We also plotted the intensity of the *Piezo2* RNAScope signal intensity as a function of the *Tmem120a* signal intensity of each individual neuron that also showed staining with the neuronal markers (Fig. 3, C, F, I, and L). Each neuronal subpopulation displayed cells with different *Tmem120a*/*Piezo2* ratios, with a tendency of having cell populations with higher *Piezo2* and lower *Tmem120a*, as well as higher *Tmem120a* and lower *Piezo2* expression levels. *Th* positive cells had relatively large proportions of high *Piezo2* low *Tmem120a* expressing cells, which are consistent with their roles as low-threshold mechanoreceptors (Le Pichon and Chesler, 2014). *Nefh* positive neurons showed a similar, but less pronounced trend, which is consistent with many of these neurons serving as low-threshold mechanoreceptors or proprioceptors (Le Pichon and Chesler, 2014). *Trpv1* and *Calcb* positive neurons, on the other hand, had more neurons with low *Piezo2* and high *Tmem120a*, consistent with these neurons being nociceptors and not playing major roles in mechanosensation, or having high mechanical thresholds (Le Pichon and Chesler, 2014). These data suggest that *Tmem120a*/*Piezo2* ratios may be a determinant of *Piezo2* current levels.

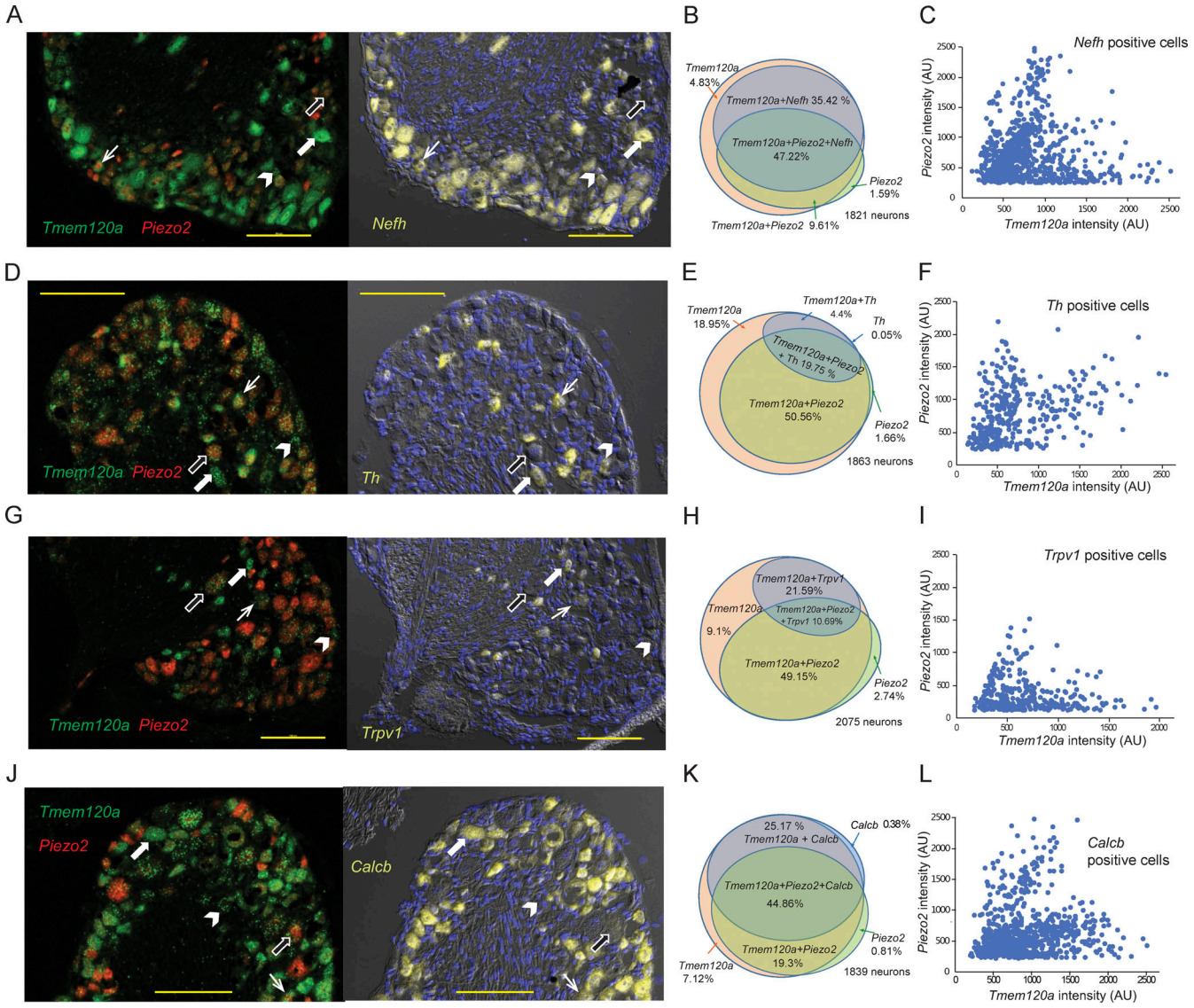

Figure 3. ***Tmem120a* and *Piezo2* are coexpressed in various DRG populations.** RNAScope fluorescence in situ hybridization on mouse DRGs was performed as described in the methods section, with probes for *Tmem120a*, *Piezo2*, and four different neuronal markers. The data represent three independent DRG preparations, and two to three slices per condition for each preparation. Arrows in representative images show cells that express: *Tmem120a* and neuronal marker (white wide arrow), *Tmem120a* and *Piezo2* and neuronal marker (white arrow), *Tmem120a* (arrowhead), and *Tmem120a* + *Piezo2* (black wide arrow). Horizontal yellow lines indicate 100 µm on each image. **(A)** Left panel: Representative image for DRGs labeled with *Tmem120a* (green) and *Piezo2* (red). Right panel: The same section labeled with *Nefh* (yellow). The section was also stained with DAPI to label nuclei. **(B)** Venn diagram showing coexpression of *Tmem120a*, *Piezo2*, and *Nefh*. **(C)** Intensity of *Piezo2* labeling as a function of *Tmem120a* signal for individual cells that was positive for *Nefh*. For both *Tmem120a* and Piezo2, cells that were below the threshold for counting as positive for *Tmem120a* or Piezo2 are not shown. **(D)** Representative images for DRGs labeled with *Tmem120a* (green) and Piezo2 (red) and *Th* (yellow). **(E)** Venn diagram showing coexpression of *Tmem120a*, *Piezo2*, and *Th*. **(F)** Intensity of Piezo2 labeling as a function of *Tmem120a* signal for individual cells that were positive for *Th*. **(G)** Representative images for DRGs labeled with *Tmem120a* (green) and Piezo2 (red) and *Trpv1* (yellow). **(H)** Venn diagram showing coexpression of *Tmem120a*, *Piezo2*, and *Trpv1*. **(I)** Intensity of Piezo2 labeling as a function of *Tmem120a* signal for individual cells that were positive for *Trpv1*. **(J)** Representative images for DRGs labeled with *Tmem120a* (green) and *Piezo2* (red) and *Calcb* (CGRP2; yellow). **(K)** Venn diagram showing coexpression of *Tmem120a*, *Piezo2*, and *Calcb*. **(L)** Intensity of *Piezo2* labeling as a function of *Tmem120a* signal for individual cells that was positive for *Calcb*. AU, arbitrary units.

To assess the role of endogenous TMEM120A, we transfected isolated DRG neurons with fluorescently labeled siRNA against *Tmem120a*, or noncoding control siRNA. We patched cells that displayed red fluorescence, and mechanically stimulated them with a blunt glass probe. We found that the amplitudes of the rapidly adapting currents were higher in the *Tmem120a* siRNA group compared to the control group (Fig. 4, A–D), which is compatible with TMEM120A acting as a negative regulator of PIEZO2 in DRG neurons. The difference was more pronounced at low-indentation depths, where much fewer cells responded in the control group compared to the *Tmem120a* siRNA group (Fig. 4 C). Consistent with this, the thresholds for mechanical activation of rapidly adapting MA in neurons transfected with *Tmem120a* siRNA were also significantly lower than in the sham siRNA

group (Fig. 4 E). There was no difference in the inactivation time constants (Fig. S7 A) or the cell capacitance (Fig. S7 B) between the *Tmem120a* siRNA group and control. *Tmem120a* siRNA did not change the proportion of the rapid, intermediate, and slowly adapting mechanically activated currents in DRG neurons (Fig. 4, F and G). To assess the efficiency of the siRNA against *Tmem120a*, we transfected *Piezo1* deficient N2A cells with siRNA against *Tmem120a* and found a statistically significant ∼30% decrease at the protein level by Western blot compared to sham siRNA (Fig. S7, C and D). Given that the transfection efficiency in N2A cells was ∼50% based on the number of fluorescent cells, the knockdown of *Tmem120a* in individual cells that took up the siRNA is likely to be around 60% at the protein level.

Overall our data show that TMEM120A inhibits the activity of PIEZO2 channels when the two proteins are heterologously expressed together, and endogenous TMEM120A inhibits the activity of endogenous PIEZO2 currents in DRG neurons.

Discussion

Here, we report that TMEM120A inhibits mechanically activated PIEZO2 channels. TMEM120A was proposed to function as an ion channel responsible for slowly adapting mechanically activated currents in DRG neurons. Overexpression of *Tmem120a* increased the amplitudes of currents evoked by negative pressure applied through the patch pipette in the cell-attached configuration in several cell lines (Beaulieu-Laroche et al., 2020). These currents, however, were very small, only 1–2 pA on average, approximately doubling the amplitudes of background currents observed in mock transfected cells (Beaulieu-Laroche et al., 2020). In our hands, overexpression of *Tmem120a* in *Piezo1* deficient N2A cells did not increase the amplitudes of currents evoked by negative pressures over background levels in the cell-attached configuration, but overexpression of *Piezo1* with or without *Tmem120a* induced a 5.5-fold increase over background current levels. The lack of appearance of mechanically activated currents after *Tmem120a* expression is consistent with several recent publications (Niu et al., 2021; Rong et al., 2021; Xue et al., 2021). Overexpression of *Tmem120a*, on the other hand, evoked a robust decrease in *Piezo2* currents evoked by indentation of the cell membrane with a blunt glass probe in the whole-cell configuration. Interestingly, a recent paper showed that expressing the M207A mutant of *Tmem120a* resulted in a sixfold increase in mechanically activated currents compared to mock transfected cells, while wild-type *Tmem120a* expressing cells were not markedly different from mock-transfected controls (Chen et al., 2022).

In the whole-cell configuration, neither the original publication describing TMEM120A (TACAN; Beaulieu-Laroche et al., 2020), nor we, observed increased mechanically activated currents after overexpression of *Tmem120a*. Treatment of DRG neurons in the *Trpv1* lineage with siRNA against *Tmem120a*, on the other hand, decreased the proportion of mechanically activated currents with ultra-slow inactivation kinetics in the whole-cell configuration (Beaulieu-Laroche et al., 2020). In our hands, *Tmem120a* siRNA had no significant effect on the proportion of slowly adapting MA currents, which is consistent with a recent report, which found no effect of *Tmem120a* siRNA on the proportion and amplitudes of slowly and ultra-slowly adapting currents (Parpaite et al., 2021). *Tmem120a* siRNA, on the other hand, increased the amplitudes of rapidly adapting MA currents in DRG neurons, which is consistent with TMEM120A suppressing PIEZO2 activity. In recent single-cell RNA sequencing experiments, *Tmem120a* was found to have the highest expression in a subpopulation of DRG neurons that did not respond to mechanical indentation, also raising doubts about TMEM120A serving as a mechanically activated ion channel in DRG neurons (Michel et al., 2020).

TMEM120A was shown by immunohistochemistry to be present predominantly in small nonpeptidergic DRG neurons with a significant expression also in tyrosine hydroxylase positive neurons, but no expression in myelinated NF200 neurons (Beaulieu-Laroche et al., 2020). A recent report, however, showed a broader expression of *Tmem120a*, with substantial expression also in myelinated DRG neurons (Parpaite et al., 2021). In our hands, *Tmem120a* expression with RNAScope in situ hybridization was detected in more than 90% of neurons, both in cells expressing a marker of myelinated neurons, and in neurons expressing *Calcb* (CGRP2), *Trpv1*, or *Th*. *Tmem120a* and *Piezo2* expression also showed substantial overlap, with varying *Tmem120a/Piezo2* ratios, indicating that TMEM120A may, in principle, be an important determinant of PIEZO2 activity in DRG neurons. Consistent with this, we found that siRNA-mediated knockdown of *Tmem120a* increased the amplitudes of rapidly adapting mechanically activated currents in DRG neurons. The effect was more pronounced at lower indentation depths, and the mechanical threshold was shifted to the left in neurons transfected with *Tmem120a* siRNA. When we plotted the maximal current amplitudes before the seals were lost, the difference between the *Tmem120a* siRNA group and the control was not statistically significant ($P = 0.15$, data not shown), consistent with a recent report (Parpaite et al., 2021).

The effect of *Tmem120a* siRNA on current amplitudes (∼50%) was substantially smaller than the almost complete elimination of the currents by overexpression of *Tmem120a*, indicating that endogenous TMEM120A exerts a smaller effect than overexpressed TMEM120A. The relatively small increase in current can also be partly due to incomplete knockdown of TMEM120A by the siRNA at the protein level. *Tmem120a* overexpression reduced PIEZO2 current amplitudes, shifted the thresholds towards stronger mechanical stimuli, and reduced the number of cells responding to mechanical stimuli. A large fraction of the reduction in current amplitudes comes from the lack of responsiveness of many *Tmem120a* expressing cells. It is hard to tell if the nonresponding cells would have displayed MA currents if the seals would have stayed intact for deeper indentations, and if they responded what the maximum currents would have been. This hinders drawing firm conclusions on the mechanism of inhibition when *Tmem120a* is overexpressed. The common observation between siRNA knockdown and overexpression of *Tmem120a* was the shifted threshold of mechanical activation, suggesting that this may be the primary effect of TMEM120A. It is possible therefore that the lack of responsiveness was due to a large shift in threshold to mechanical

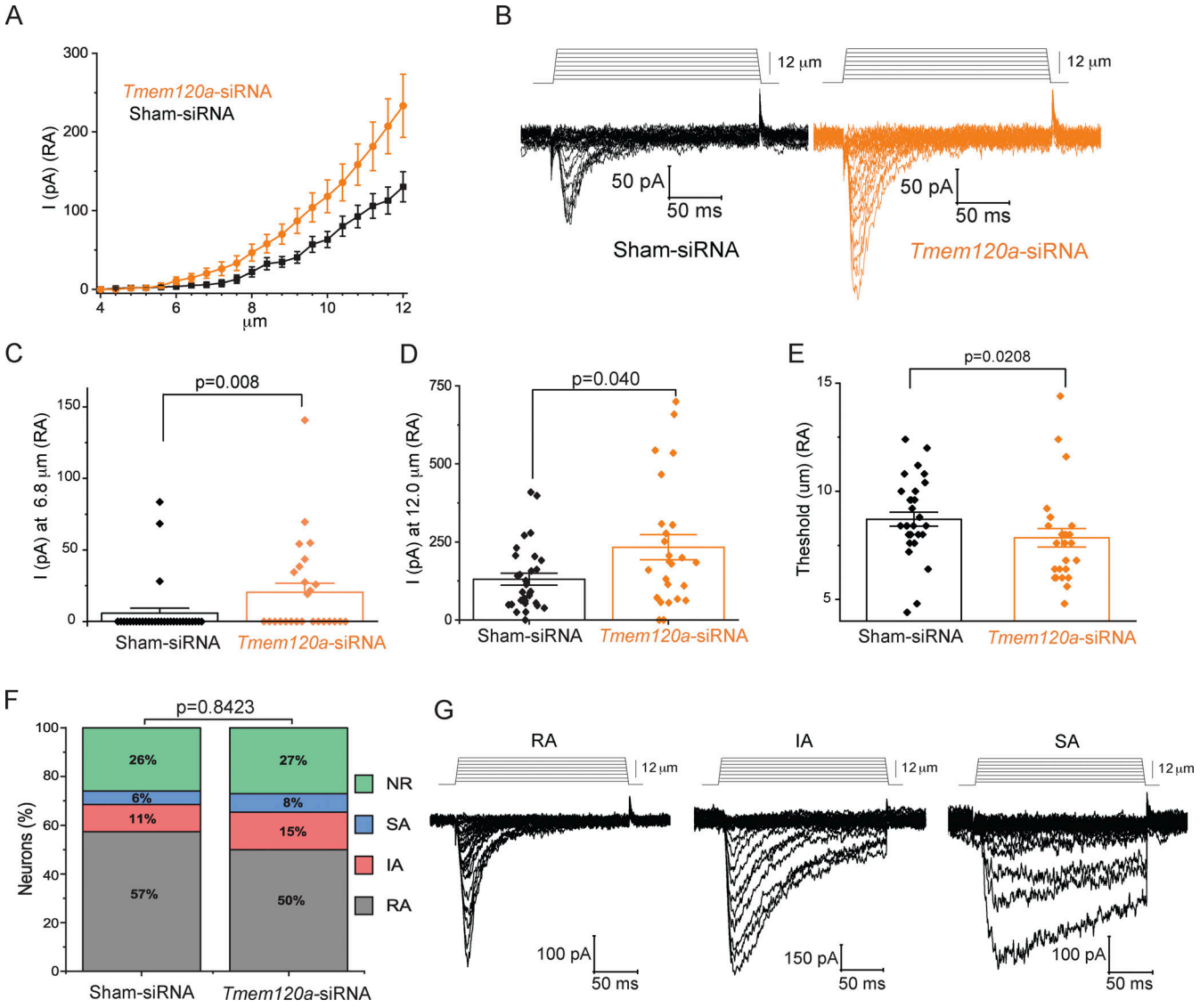

Figure 4. **TMEM120A negatively regulates rapidly adapting mechanically activated currents in mouse DRG neurons.** Mouse DRG neurons were transfected with *Tmem120a*-siRNA or nontargeting negative control siRNA (Sham-siRNA) as described in the Materials and methods section. Whole-cell patch-clamp experiments were performed at −60 mV with mechanically activated currents evoked by increasing indentation with a blunt glass probe. **(A)** DRG neurons with rapidly adapting (RA) inactivation kinetics indicative of native Piezo2 were measured. Current amplitudes are plotted (mean ± SEM) for Sham-siRNA neurons with RA kinetics (black) and for *Tmem120a* -siRNA neurons with RA kinetics (orange). **(B)** Representative RA-type current traces. **(C and D)** Scatter plots and mean ± SEM for current amplitudes at 6.8 and 12.0 μm indentations. **(E)** Scatter plots and mean ± SEM for mechanical threshold (blunt glass probe indentation depth required to elicit RA type currents). **(F)** Percentage of cells displaying RA, intermediate adapting (IA), and slow adapting (SA) currents and nonresponding neurons (NR) for those transfected with Sham-siRNA and *Tmem120a* -siRNA. The electrophysiology data are from four independent DRG neuron preparations and transfections, n = 54 for Sham-siRNA, and n = 52 for *Tmem120a* -siRNA. Statistical significance was assessed using the chi-squared test. **(G)** Representative RA, IA, and SA current traces. Statistical significance for C–E was calculated with the Mann-Whitney test.

forces that cannot be attained without disrupting seal integrity in a large fraction of cells.

When *Tmem120a* was conditionally knocked out from non-peptidergic DRG neurons that express *Mrgprd* in a tamoxifen-inducible fashion, mice showed reduced nocifensive responses to von-Frey filaments (greater or equal to 1 g), but they retained reflexive withdrawal (Beaulieu-Laroche et al., 2020). Paw withdrawal from painful pinprick stimuli, on the other hand, was not affected by *Tmem120a* deletion (Beaulieu-Laroche et al., 2020). *Tmem120a* knockdown by spinal intrathecal injection of antisense oligodeoxynucleotides into rats, reduced inflammatory, but not chemotherapy-induced mechanical hyperalgesia (Bonet et al., 2020). These data support the idea that TMEM120A regulates some, but not all forms of mechanonociception.

Our data, however, indicate that TMEM120A inhibits PIEZO2 currents. Can this be reconciled with the behavioral findings in *Tmem120a* deficient mice? As mentioned earlier, the role of PIEZO2 in detecting noxious mechanical stimuli is complex. One study found that paradoxically, conditional deletion of *Piezo2* in DRG neurons using an Advillin-cre mouse line reduced the threshold to painful mechanical stimuli in the Randall-Selitto test, even though the mice had defective gentle touch (Zhang

et al., 2019). Ectopic expression of *Piezo1* in DRG neurons, on the other hand, decreased sensitivity in the Randall-Selitto test (Zhang et al., 2019). These data indicate that activation of PIEZO2 may inhibit mechanical pain. This is compatible with classical gate control theory of pain (Melzack and Wall, 1965), where stimulation of light touch receptors reduces pain. In this framework, increasing PIEZO2-mediated currents by *Tmem120a* knockdown can potentially reduce pain.

What is the mechanism of PIEZO2 inhibition by TMEM120A? *Tmem120a* coexpression did not significantly change TIRF signal for GFP-PIEZO2, suggesting that TMEM120A does not decrease cell-surface expression of PIEZO2. While TIRF illuminates not only the plasma membrane but also a narrow subplasmalemmal cytoplasmic region, given the exponential decay of the illumination intensity by distance, a displacement of a large fraction of PIEZO2 from the plasma membrane to the cytoplasm should be detectable with TIRF even if the channel remains close to the plasma membrane. The increase in the mechanical threshold of PIEZO2 when TMEM120A is present also argues against decreased surface expression being the major mechanism of inhibition, which would be expected to evoke a similar decrease of currents at every stimulation level. While TIRF imaging does not have sufficient resolution to detect protein–protein interaction, the weak colocalization of TMEM120A with PIEZO2 makes it unlikely that the mechanism is direct interaction with the channel. TMEM120A also did not induce a major reorganization of the actin and tubulin cytoskeleton, and it did not inhibit the activity of two other mechanosensitive channels PIEZO1 and TREK1. These data indicate that the inhibition of PIEZO2 is not due to a general change in mechanical properties of the cell, or a general decrease of the ability of the cell to transduce mechanical forces to ion channels.

TMEM120A was also characterized earlier as a fat-specific nuclear envelope transmembrane protein 29 (Malik et al., 2010; Batrakou et al., 2015), and it was shown that its overexpression can alter gene expression (de Las Heras et al., 2017). Thus, it is possible that TMEM120A increases or decreases the expression of other proteins that regulate PIEZO2 properties. Consistent with its reported nuclear envelope localization, we also find that substantial amount of TMEM120A is intracellular.

Recent publications showed that the structure of TMEM120A determined by cryo-EM showed similarity to the fatty acid elongase ELOVL7, and the structure of TMEM120A also contained a coenzyme-A molecule (Niu et al., 2021; Rong et al., 2021; Xue et al., 2021). PIEZO2 as well as PIEZO1 were shown to be regulated by a variety of lipids (Borbiro et al., 2015; Narayanan et al., 2018; Romero et al., 2019; Romero et al., 2020), therefore it is possible that TMEM120A modulates PIEZO2 activity through modifying the lipid content of the cell. Exploring this possibility will require future research efforts characterizing lipid changes induced by TMEM120A and identifying potential lipid species that modify the function of PIEZO2.

Acknowledgments

Jeanne M. Nerbonne served as editor.

The *Piezo1* IRES GFP and the *Piezo2* pcDNA clones were kind gifts from Dr. Ardem Patapoutian, Scripps Research. The Piezo1 deficient Neuro2A cell line was a kind gift from Dr. Valeria Vasquez (University of Tennessee Health Science Center, Memphis, TN) with permission from Dr. Gary Lewin (Max Delbruck Center for Molecular Medicine, Berlin, Germany). The authors are grateful to Dr. Sabine Hilfiker for giving access to her Olympus confocal microscope, and to Rachel Fasiczka for help with this microscope.

This study was supported by National Institutes of Health grants R01-NS055159 to T. Rohacs and F31-NS100484 and F99-NS113422 to J.S. Del Rosario.

The authors declare no competing financial interests.

Author contributions: J.S. Del Rosario, M. Gabrielle, and Y. Yudin conceived, designed and performed the experiments, analyzed and visualized the data, and reviewed and edited the manuscript. T. Rohacs supervised the project, conceived and designed experiments, analyzed and visualized the data, and wrote and edited the manuscript. All authors approved the final version of the manuscript.

Submitted: 28 March 2022
Accepted: 24 June 2022

References

Anderson, E.O., E.R. Schneider, J.D. Matson, E.O. Gracheva, and S.N. Bagriantsev. 2018. TMEM150C/Tentonin3 is a regulator of mechano-gated ion channels. *Cell Rep.* 23:701–708. https://doi.org/10.1016/j.celrep.2018.03.094

Assaraf, E., R. Blecher, L. Heinemann-Yerushalmi, S. Krief, R. Carmel Vinestock, I.E. Biton, V. Brumfeld, R. Rotkopf, E. Avisar, G. Agar, and E. Zelzer. 2020. Piezo2 expressed in proprioceptive neurons is essential for skeletal integrity. *Nat. Commun.* 11:3168. https://doi.org/10.1038/s41467-020-16971-6

Batrakou, D.G., J.I. de Las Heras, R. Czapiewski, R. Mouras, and E.C. Schirmer. 2015. TMEM120A and B: Nuclear envelope transmembrane proteins important for adipocyte differentiation. *PLoS One.* 10:e0127712. https://doi.org/10.1371/journal.pone.0127712

Beaulieu-Laroche, L., M. Christin, A. Donoghue, F. Agosti, N. Yousefpour, H. Petitjean, A. Davidova, C. Stanton, U. Khan, C. Dietz, et al. 2020. TACAN is an ion channel involved in sensing mechanical pain. *Cell.* 180:956–967.e17. https://doi.org/10.1016/j.cell.2020.01.033

Besch, S.R., T. Suchyna, and F. Sachs. 2002. High-speed pressure clamp. *Pflugers Arch.* 445:161–166. https://doi.org/10.1007/s00424-002-0903-0

Bonet, I.J.M., D. Araldi, O. Bogen, and J.D. Levine. 2021. Involvement of TACAN, a mechanotransducing ion channel, in inflammatory but not neuropathic hyperalgesia in the rat. *The J. Pain.* 22:498–508. https://doi.org/10.1016/j.jpain.2020.11.004

Borbiro, I., D. Badheka, and T. Rohacs. 2015. Activation of TRPV1 channels inhibits mechanosensitive Piezo channel activity by depleting membrane phosphoinositides. *Sci. Signal.* 8:ra15. https://doi.org/10.1126/scisignal.2005667

Chang, W., and J.G. Gu. 2020. Role of microtubules in Piezo2 mechanotransduction of mouse Merkel cells. *J. Neurophysiol.* 124:1824–1831. https://doi.org/10.1152/jn.00502.2020

Chen, X., Y. Wang, Y. Li, X. Lu, J. Chen, M. Li, T. Wen, N. Liu, S. Chang, X. Zhang, et al. 2022. Cryo-EM structure of the human TACAN in a closed state. *Cell Rep.* 38:110445. https://doi.org/10.1016/j.celrep.2022.110445

Chesler, A.T., M. Szczot, D. Bharucha-Goebel, M. Ceko, S. Donkervoort, C. Laubacher, L.H. Hayes, K. Alter, C. Zampieri, C. Stanley, et al. 2016. The role of PIEZO2 in human mechanosensation. *N. Engl. J. Med.* 375:1355–1364. https://doi.org/10.1056/NEJMoa1602812

Coste, B., J. Mathur, M. Schmidt, T.J. Earley, S. Ranade, M.J. Petrus, A.E. Dubin, and A. Patapoutian. 2010. Piezo1 and Piezo2 are essential components of distinct mechanically activated cation channels. *Science.* 330:55–60. https://doi.org/10.1126/science.1193270

de Las Heras, J.I., N. Zuleger, D.G. Batrakou, R. Czapiewski, A.R.W. Kerr, and E.C. Schirmer. 2017. Tissue-specific NETs alter genome organization

and regulation even in a heterologous system. *Nucleus*. 8:81–97. https://doi.org/10.1080/19491034.2016.1261230

Del Rosario, J.S., Y. Yudin, S. Su, C.M. Hartle, T. Mirshahi, T. Rohacs, and T. Rohacs. 2020. Gi-coupled receptor activation potentiates Piezo2 currents via Gβγ. *EMBO Rep.* 21:e49124. https://doi.org/10.15252/embr.201949124

Dubin, A.E., S. Murthy, A.H. Lewis, L. Brosse, S.M. Cahalan, J. Grandl, B. Coste, and A. Patapoutian. 2017. Endogenous Piezo1 can confound mechanically activated channel identification and characterization. *Neuron*. 94:266–270.e3. https://doi.org/10.1016/j.neuron.2017.03.039

Ellefsen, K.L., J.R. Holt, A.C. Chang, J.L. Nourse, J. Arulmoli, A.H. Mekhdjian, H. Abuwarda, F. Tombola, L.A. Flanagan, A.R. Dunn, et al. 2019. Myosin-II mediated traction forces evoke localized Piezo1-dependent Ca(2+) flickers. *Commun. Biol.* 2:298. https://doi.org/10.1038/s42003-019-0514-3

Fish, K.N. 2009. Total internal reflection fluorescence (TIRF) microscopy. *Curr. Protoc. Cytom.* Chapter 12:Unit12.18. https://doi.org/10.1002/0471142956.cy1218s50

Gottlieb, P.A., and F. Sachs. 2012. Piezo1: Properties of a cation selective mechanical channel. *Channels*. 6:214–219. https://doi.org/10.4161/chan.21050

Hong, G.S., B. Lee, and U. Oh. 2017. Evidence for mechanosensitive channel activity of Tentonin 3/TMEM150C. *Neuron*. 94:271–273.e2. https://doi.org/10.1016/j.neuron.2017.03.038

Hong, G.S., B. Lee, J. Wee, H. Chun, H. Kim, J. Jung, J.Y. Cha, T.R. Riew, G.H. Kim, I.B. Kim, and U. Oh. 2016. Tentonin 3/TMEM150c confers distinct mechanosensitive currents in dorsal-root ganglion neurons with proprioceptive function. *Neuron*. 91:708–710. https://doi.org/10.1016/j.neuron.2016.07.019

Jia, Z., R. Ikeda, J. Ling, V. Viatchenko-Karpinski, and J.G. Gu. 2016. Regulation of Piezo2 mechanotransduction by static plasma membrane tension in primary afferent neurons. *J. Biol. Chem.* 291:9087–9104. https://doi.org/10.1074/jbc.M115.692384

Jiang, W., J.S. Del Rosario, W. Botello-Smith, S. Zhao, Y.C. Lin, H. Zhang, J. Lacroix, T. Rohacs, and Y.L. Luo. 2021. Crowding-induced opening of the mechanosensitive Piezo1 channel in silico. *Commun. Biol.* 4:84. https://doi.org/10.1038/s42003-020-01600-1

Ke, M., Y. Yu, C. Zhao, S. Lai, Q. Su, W. Yuan, L. Yang, D. Deng, K. Wu, W. Zeng, et al. 2021. Cryo-EM structures of human TMEM120A and TMEM120B. *Cell Discov.* 7:77. https://doi.org/10.1038/s41421-021-00319-5

Kefauver, J.M., A.B. Ward, and A. Patapoutian. 2020. Discoveries in structure and physiology of mechanically activated ion channels. *Nature*. 587:567–576. https://doi.org/10.1038/s41586-020-2933-1

Le Pichon, C.E., and A.T. Chesler. 2014. The functional and anatomical dissection of somatosensory subpopulations using mouse genetics. *Front. Neuroanat.* 8:21. https://doi.org/10.3389/fnana.2014.00021

Lewis, A.H., and J. Grandl. 2015. Mechanical sensitivity of Piezo1 ion channels can be tuned by cellular membrane tension. *Elife*. 4:e12088. https://doi.org/10.7554/eLife.12088

Li, Y., S. Huang, X. Li, X. Yang, N. Xu, J. Qu, and H.Y. Mak. 2021. The endoplasmic reticulum-resident protein TMEM-120/TMEM120A promotes fat storage in *C. elegans* and mammalian cells. *bioRxiv*. (Preprint posted June 29, 2021). https://doi.org/10.1101/2021.06.29.450322

Malik, P., N. Korfali, V. Srsen, V. Lazou, D.G. Batrakou, N. Zuleger, D.M. Kavanagh, G.S. Wilkie, M.W. Goldberg, and E.C. Schirmer. 2010. Cell-specific and lamin-dependent targeting of novel transmembrane proteins in the nuclear envelope. *Cell Mol. Life Sci.* 67:1353–1369. https://doi.org/10.1007/s00018-010-0257-2

Martin-Fernandez, M.L., C.J. Tynan, and S.E.D. Webb. 2013. A "pocket guide" to total internal reflection fluorescence. *J. Microsc.* 252:16–22. https://doi.org/10.1111/jmi.12070

Melzack, R., and P.D. Wall. 1965. Pain mechanisms: A new theory. *Science*. 150:971–979. https://doi.org/10.1126/science.150.3699.971

Michel, N., P. Narayanan, O. Shomroni, and M. Schmidt. 2020. Maturational changes in mouse cutaneous touch and Piezo2-mediated mechanotransduction. *Cell Rep.* 32:107912. https://doi.org/10.1016/j.celrep.2020.107912

Moroni, M., M.R. Servin-Vences, R. Fleischer, O. Sanchez-Carranza, and G.R. Lewin. 2018. Voltage gating of mechanosensitive PIEZO channels. *Nat. Commun.* 9:1096. https://doi.org/10.1038/s41467-018-03502-7

Murthy, S.E., A.E. Dubin, T. Whitwam, S. Jojoa-Cruz, S.M. Cahalan, S.A.R. Mousavi, A.B. Ward, and A. Patapoutian. 2018a. OSCA/TMEM63 are an evolutionarily conserved family of mechanically activated ion channels. *Elife*. 7:e41844. https://doi.org/10.7554/eLife.41844

Murthy, S.E., M.C. Loud, I. Daou, K.L. Marshall, F. Schwaller, J. Kuhnemund, A.G. Francisco, W.T. Keenan, A.E. Dubin, G.R. Lewin, and A. Patapoutian. 2018b. The mechanosensitive ion channel Piezo2 mediates sensitivity to mechanical pain in mice. *Sci. Translat. Med.* 10:eaat9897. https://doi.org/10.1126/scitranslmed.aat9897

Narayanan, P., M. Hutte, G. Kudryasheva, F.J. Taberner, S.G. Lechner, F. Rehfeldt, D. Gomez-Varela, and M. Schmidt. 2018. Myotubularin related protein-2 and its phospholipid substrate PIP_2 control Piezo2-mediated mechanotransduction in peripheral sensory neurons. *Elife*. 7:e32346. https://doi.org/10.7554/eLife.32346

Nie, L., T.C. Pascoa, A.C.W. Pike, S.R. Bushell, A. Quigley, G.F. Ruda, A. Chu, V. Cole, D. Speedman, T. Moreira, et al. 2021. The structural basis of fatty acid elongation by the ELOVL elongases. *Nat. Struct. Mol. Biol.* 28:512–520. https://doi.org/10.1038/s41594-021-00605-6

Niu, Y., X. Tao, G. Vaisey, P.D.B. Olinares, H. Alwaseem, B.T. Chait, and R. MacKinnon. 2021. Analysis of the mechanosensor channel functionality of TACAN. *Elife*. 10:e71188. https://doi.org/10.7554/eLife.71188

Parpaite, T., L. Brosse, N. Sejourne, A. Laur, Y. Mechioukhi, P. Delmas, and B. Coste. 2021. Patch-seq of mouse DRG neurons reveals candidate genes for specific mechanosensory functions. *Cell Rep.* 37:109914. https://doi.org/10.1016/j.celrep.2021.109914

Patkunarajah, A., J.H. Stear, M. Moroni, L. Schroeter, J. Blaszkiewicz, J.L. Tearle, C.D. Cox, C. Furst, O. Sanchez-Carranza, M.D.A. Ocana Fernandez, et al. 2020. TMEM87a/Elkin1, a component of a novel mechanoelectrical transduction pathway, modulates melanoma adhesion and migration. *Elife*. 9:e53308. https://doi.org/10.7554/eLife.53308

Ranade, S.S., S.H. Woo, A.E. Dubin, R.A. Moshourab, C. Wetzel, M. Petrus, J. Mathur, V. Begay, B. Coste, J. Mainquist, et al. 2014. Piezo2 is the major transducer of mechanical forces for touch sensation in mice. *Nature*. 516:121–125. https://doi.org/10.1038/nature13980

Ridone, P., E. Pandzic, M. Vassalli, C.D. Cox, A. Macmillan, P.A. Gottlieb, and B. Martinac. 2020. Disruption of membrane cholesterol organization impairs the activity of PIEZO1 channel clusters. *J. Gen. Physiol.* 152:e201912515. https://doi.org/10.1085/jgp.201912515

Romero, L.O., R. Caires, A.R. Nickolls, A.T. Chesler, J.F. Cordero-Morales, and V. Vasquez. 2020. A dietary fatty acid counteracts neuronal mechanical sensitization. *Nat. Commun.* 11:2997. https://doi.org/10.1038/s41467-020-16816-2

Romero, L.O., A.E. Massey, A.D. Mata-Daboin, F.J. Sierra-Valdez, S.C. Chauhan, J.F. Cordero-Morales, and V. Vasquez. 2019. Dietary fatty acids fine-tune Piezo1 mechanical response. *Nat. Commun.* 10:1200. https://doi.org/10.1038/s41467-019-09055-7

Rong, Y., J. Jiang, Y. Gao, D. Song, D. Song, W. Liu, B. Xiao, Y. Zhao, B. Xiao, and Z. Liu. 2021. TMEM120A contains a specific coenzyme A-binding site and might not mediate poking- or stretch-induced channel activities in cells. *Elife*. 10:e71474. https://doi.org/10.7554/eLife.71474

Shin, K.C., H.J. Park, J.G. Kim, I.H. Lee, H. Cho, C. Park, T.S. Sung, S.D. Koh, S.W. Park, and Y.M. Bae. 2019. The Piezo2 ion channel is mechanically activated by low-threshold positive pressure. *Sci. Rep.* 9:6446. https://doi.org/10.1038/s41598-019-42492-4

Su, S., Y. Yudin, N. Kim, Y.X. Tao, and T. Rohacs. 2021. TRPM3 channels play roles in heat hypersensitivity and spontaneous pain after nerve injury. *J. Neurosci.* 41:2457–2474. https://doi.org/10.1523/JNEUROSCI.1551-20.2020

Szczot, M., L.A. Pogorzala, H.J. Solinski, L. Young, P. Yee, C.E. Le Pichon, A.T. Chesler, and M.A. Hoon. 2017. Cell-type-specific splicing of Piezo2 regulates mechanotransduction. *Cell Rep.* 21:2760–2771. https://doi.org/10.1016/j.celrep.2017.11.035

Usoskin, D., A. Furlan, S. Islam, H. Abdo, P. Lonnerberg, D. Lou, J. Hjerling-Leffler, J. Haeggstrom, O. Kharchenko, P.V. Kharchenko, et al. 2015. Unbiased classification of sensory neuron types by large-scale single-cell RNA sequencing. *Nat. Neurosci.* 18:145–153. https://doi.org/10.1038/nn.3881

Wu, J., M. Young, A.H. Lewis, A.N. Martfeld, B. Kalmeta, and J. Grandl. 2017. Inactivation of mechanically activated Piezo1 ion channels is determined by the C-terminal extracellular domain and the inner pore helix. *Cell Rep.* 21:2357–2366. https://doi.org/10.1016/j.celrep.2017.10.120

Xue, J., Y. Han, H. Baniasadi, W. Zeng, J. Pei, N.V. Grishin, J. Wang, B.P. Tu, and Y. Jiang. 2021. TMEM120A is a coenzyme A-binding membrane protein with structural similarities to ELOVL fatty acid elongase. *Elife*. 10:e71220. https://doi.org/10.7554/eLife.71220

Yamamura, H., Y. Suzuki, and Y. Imaizumi. 2015. New light on ion channel imaging by total internal reflection fluorescence (TIRF) microscopy. *J. Pharmacol. Sci.* 128:1–7. https://doi.org/10.1016/j.jphs.2015.04.004

Zhang, M., Y. Wang, J. Geng, S. Zhou, and B. Xiao. 2019. Mechanically activated piezo channels mediate touch and suppress acute mechanical pain response in mice. *Cell Rep.* 26:1419–1431.e4. https://doi.org/10.1016/j.celrep.2019.01.056

Supplemental material

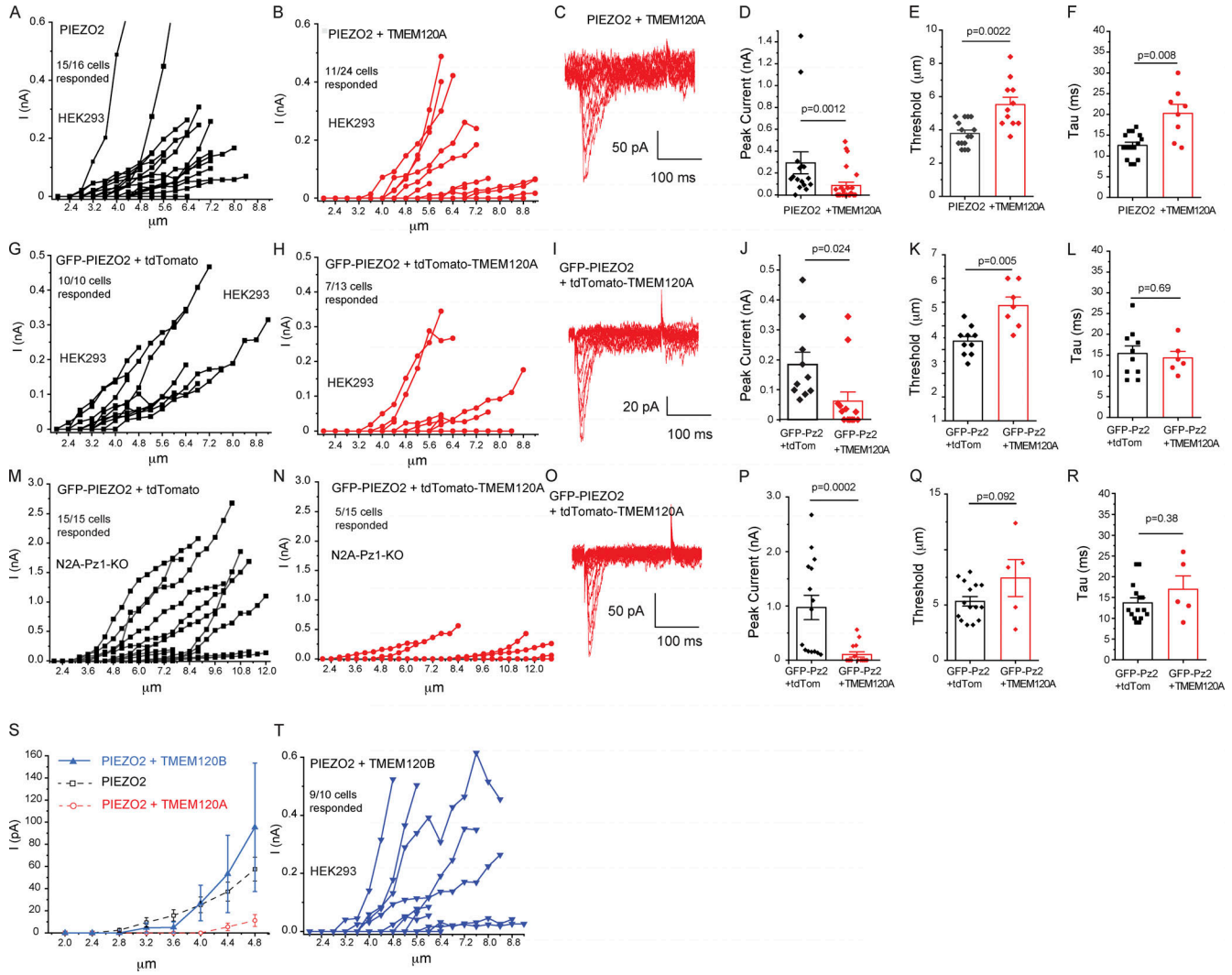

Figure S1. **TMEM120A but not TMEM120B inhibits PIEZO2 currents.** Data from Fig. 1 showing the full range of measurements with indentation depth increased until seals were lost. **(A and B)** Data from HEK293 cells transfected with *Piezo2* and *Tmem120A*. **(C)** Representative traces for increasing indentation depth till 7.2 µm. **(D)** Peak current amplitudes regardless of indentation depth. **(E)** Mechanical threshold of responding cells. **(F)** Inactivation time constant (tau). **(G and H)** Data from HEK293 cells transfected with GFP-*Piezo2* and tdTomato-*Tmem120A*. **(I)** Representative traces for indentation depths till 8.4 µm. **(J)** Peak current amplitudes regardless of indentation depth. **(K)** Mechanical threshold of responding cells. **(L)** Inactivation time constant (tau). **(M and N)** Data from *Piezo1* deficient N2A cells transfected with GFP-*Piezo2* and tdTomato-*Tmem120A*. **(O)** Representative traces for indentation depths till 11.6 µm. **(P)** Peak current amplitudes regardless of indentation depth. **(Q)** Mechanical threshold of responding cells. **(R)** Inactivation time constant (tau). **(S)** Whole-cell patch-clamp data from HEK293 cells transfected with *Piezo2* and *Tmem120B*, mean ± SEM of current amplitudes as a function of indentation depth. For PIEZO2 alone and PIEZO2 + TMEM120A data were replotted from Fig. 1 (dashed lines). **(T)** Data for full the range of indentations. Statistical significance was calculated with two-sample *t* test (F, K, L, and Q) or Mann-Whitney test (D, E, J, P, and R). Data are shown as mean ± SEM and scatter plots.

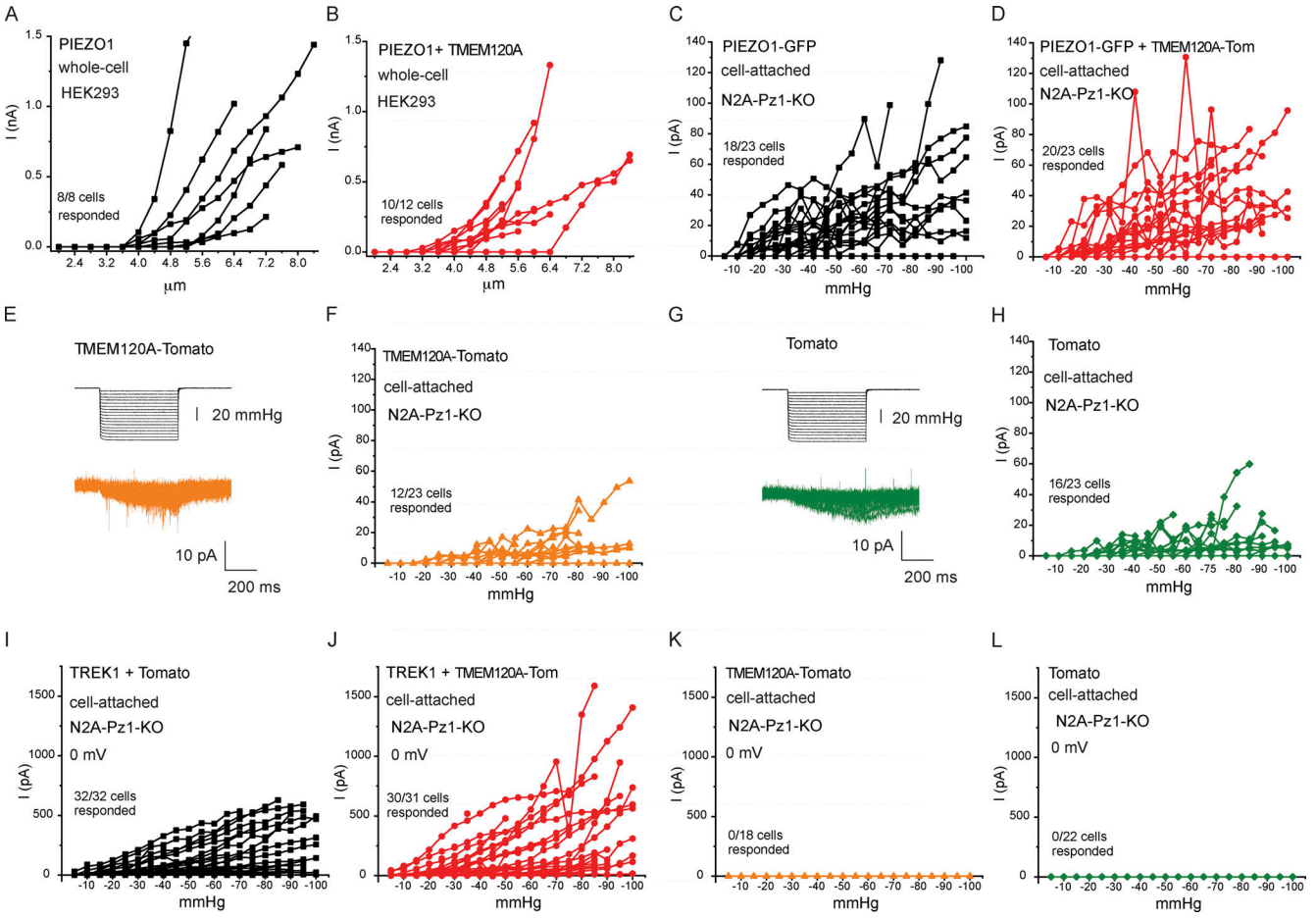

Figure S2. **TMEM120A does not inhibit PIEZO1 and TREK1 currents.** Data from Fig. 2 showing the full range of measurements with indentation depth or negative pressure increased until the seal was lost. **(A and B)** Data from whole-cell patch-clamp experiments in HEK293 cells transfected with *Piezo1* alone or *Tmem120a* + *Piezo1*. **(C and D)** Data from cell-attached patch clamp experiments in *Piezo1* deficient N2A cells transfected with *Piezo1* alone or *Tmem120a* + *Piezo1*. **(E)** Representative traces for cell-attached patch clamp experiments in N2A cell transfected with tdTomato-*Tmem120a*. **(F)** Full range of data from cell-attached patch-clamp experiments in N2A cell transfected with tdTomato-*Tmem120a*. **(G)** Representative traces for cell-attached patch-clamp experiments in N2A cell transfected with tdTomato. **(H)** Full range of data from cell-attached patch-clamp experiments in N2A cells transfected with tdTomato. **(I–L)** Full range of data from cell-attached patch-clamp experiments at 0 mV in N2A cells transfected with TREK1 + tdTomato (I), TREK1 + tdTomato-*Tmem120a* (J), tdTomato-*Tmem120a* alone (K), and tdTomato alone (L). The slight discrepancy in the number of cells compared to Fig. 2 in C, D, F, and I–L is because these panels include cells where the seal was lost before the negative pressure reached 55 mmHg, and those cells were excluded from Fig. 2.

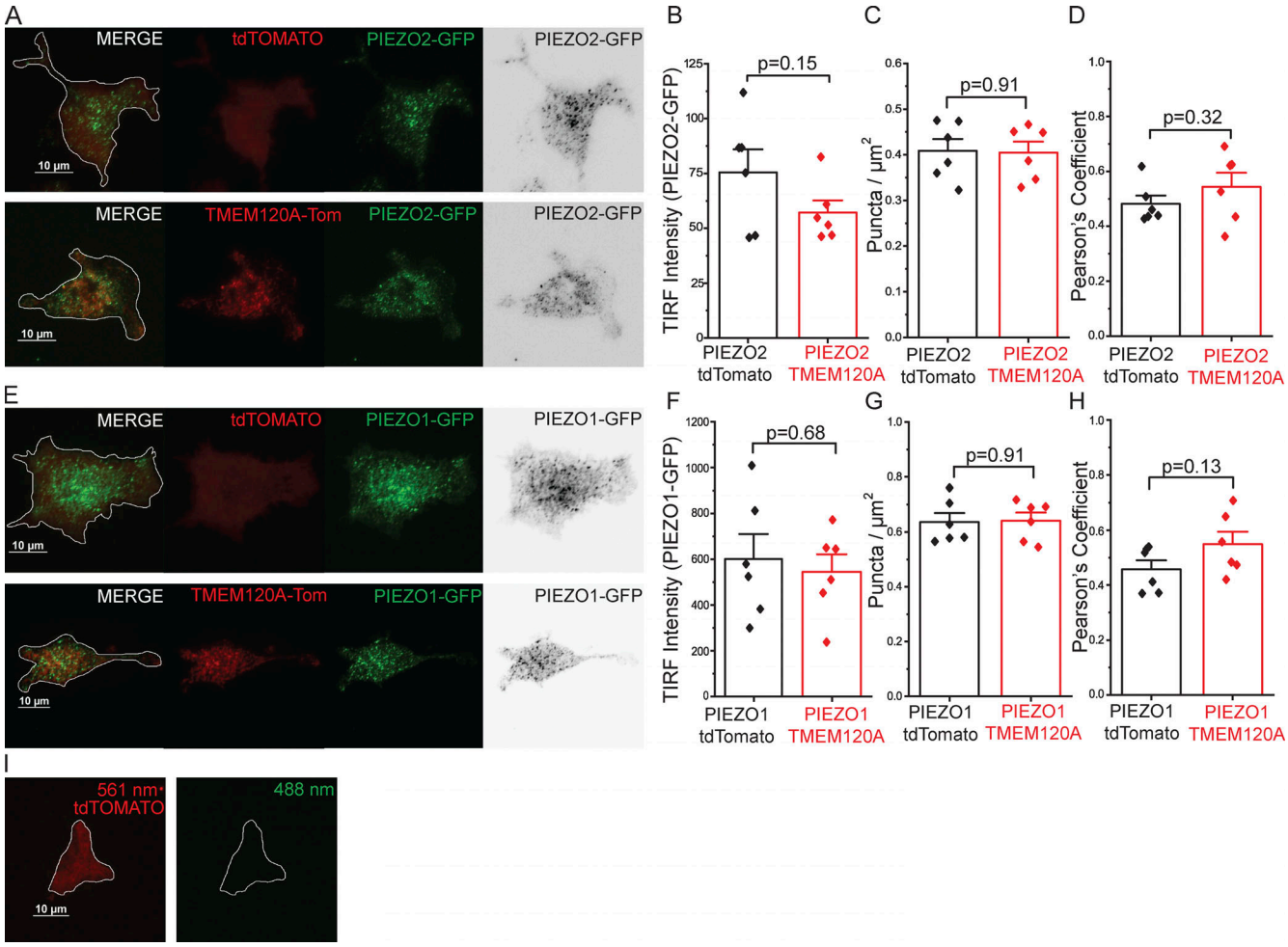

Figure S3. **TMEM120A shows only weak colocalization with PIEZO1 or PIEZO2, and does not change their cell-surface expression.** TIRF microscopy was performed as described in the Materials and methods section. **(A)** Representative TIRF images for HEK293 cell transfected with tdTomato-*Tmem120a* and GFP-*Piezo2* (bottom) and tdTomato and GFP-*Piezo2* (top). **(B)** Summary data for the fluorescence intensity for GFP-PIEZO2 in the TIRF mode for cells co-transfected with tdTomato or tdTomato-*Tmem120a*. **(C)** Number of GFP-PIEZO2 puncta per µm. **(D)** Pearson's coefficient for colocalization of tdTomato-TMEM120A with GFP-PIEZO2 and tdTomato with GFP-PIEZO2. **(E)** Representative TIRF images for HEK293 cell transfected with tdTomato-*Tmem120a* and GFP-*Piezo1* (bottom) and tdTomato and GFP-*Piezo1* (top). **(F)** Summary data for the fluorescence intensity for GFP-PIEZO1 in the TIRF mode for cell co-transfected with tdTomato or tdTomato-*Tmem120a*. **(G)** Number of GFP-PIEZO1 puncta per µm. **(H)** Pearson's coefficient for colocalization of tdTomato-TMEM120A with GFP-PIEZO1 and tdTomato with GFP-PIEZO1. **(I)** Representative image of cell expressing only tdTomato with 561-nm laser (left) and 488-nm laser (right). Bar graphs show mean ± SEM and scatter plots. Individual symbols show the average value of cells for one coverslip (5–22 cells/coverslip) from two independent transfection. Statistical significance was calculated with two-sample *t* test.

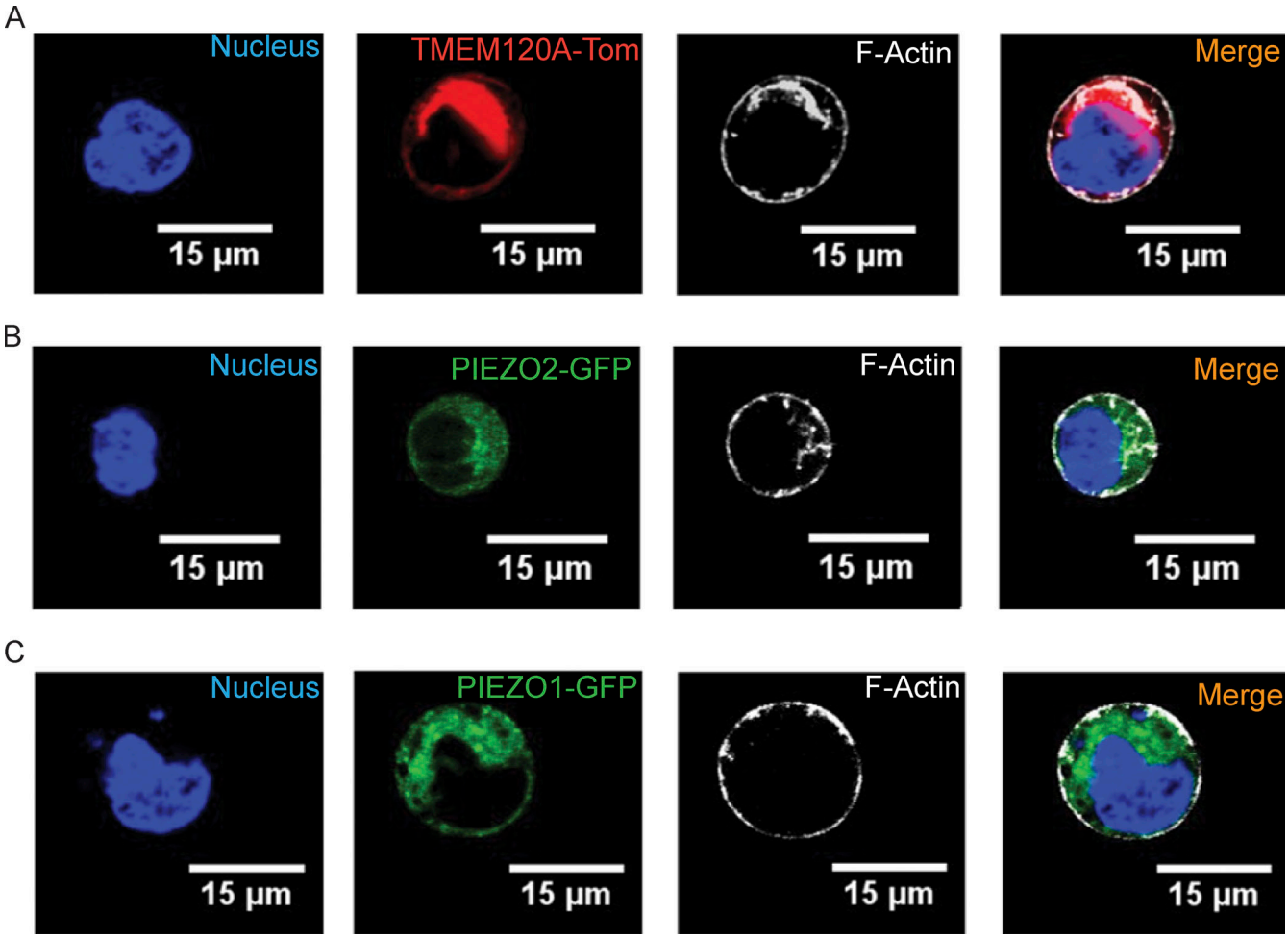

Figure S4. **TMEM120A is broadly distributed throughout cells.** HEK293 cells were transfected with tdTomato-*Tmem120a*, GFP-*Piezo1* or GFP-*Piezo2*, labeled with Sir-Actin, and confocal images were obtained as described in the Materials and methods section. **(A)** Representative confocal images of tdTomato-TMEM120A and Sir-Actin. **(B)** Representative confocal images of GFP-PIEZO2 and Sir-Actin, which labels F-Actin. **(C)** Representative confocal images of GFP-PIEZO1 and Sir-Actin. Two independent transfections were performed and 26–30 cells per group were imaged.

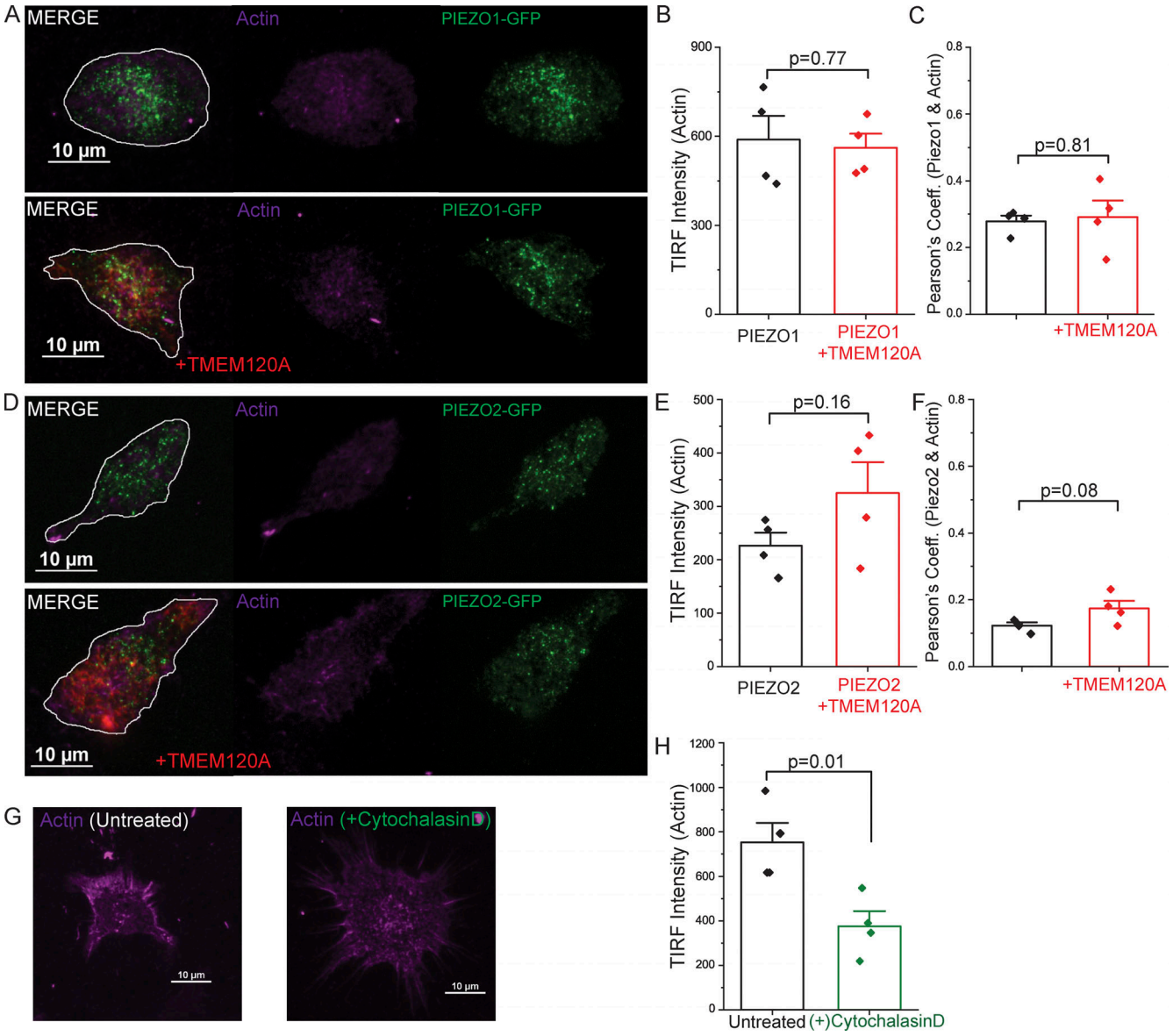

Figure S5. **TMEM120A does not affect the actin cytoskeleton.** HEK293 cells were transfected with tdTomato-*Tmem120A* and GFP-*Piezo1* or GFP-*Piezo2*, labeled with Sir-Actin, and TIRF images were obtained as described in the Materials and methods section. **(A)** Representative TIRF images for GFP-PIEZO1 and Sir-Actin. Cell outlines displayed in white on merged images. **(B)** TIRF intensity of Sir-Actin with and without TMEM120A. **(C)** Pearson's coefficient for co-localization of GFP-PIEZO1 and Sir-Actin with and without TMEM120A. **(D)** Representative TIRF images for GFP-PIEZO2 and Sir-Actin. Cell outlines displayed in white on merged images. **(E)** TIRF intensity of Sir-Actin with and without TMEM120A. **(F)** Pearson's coefficient for colocalization of GFP-PIEZO2 and Sir-Actin with and without TMEM120A. **(G)** Representative TIRF images for Sir-Actin in untreated and cytochalasin D treated cells. **(H)** TIRF intensity of Sir-Actin with and without cytochalasin D treatment. Bar graphs show mean ± SEM and scatter plots. Individual symbols show the average value of cells for one coverslip (5–22 cells/coverslip) from two independent transfections. Statistical significance was calculated with the two-sample *t* test.

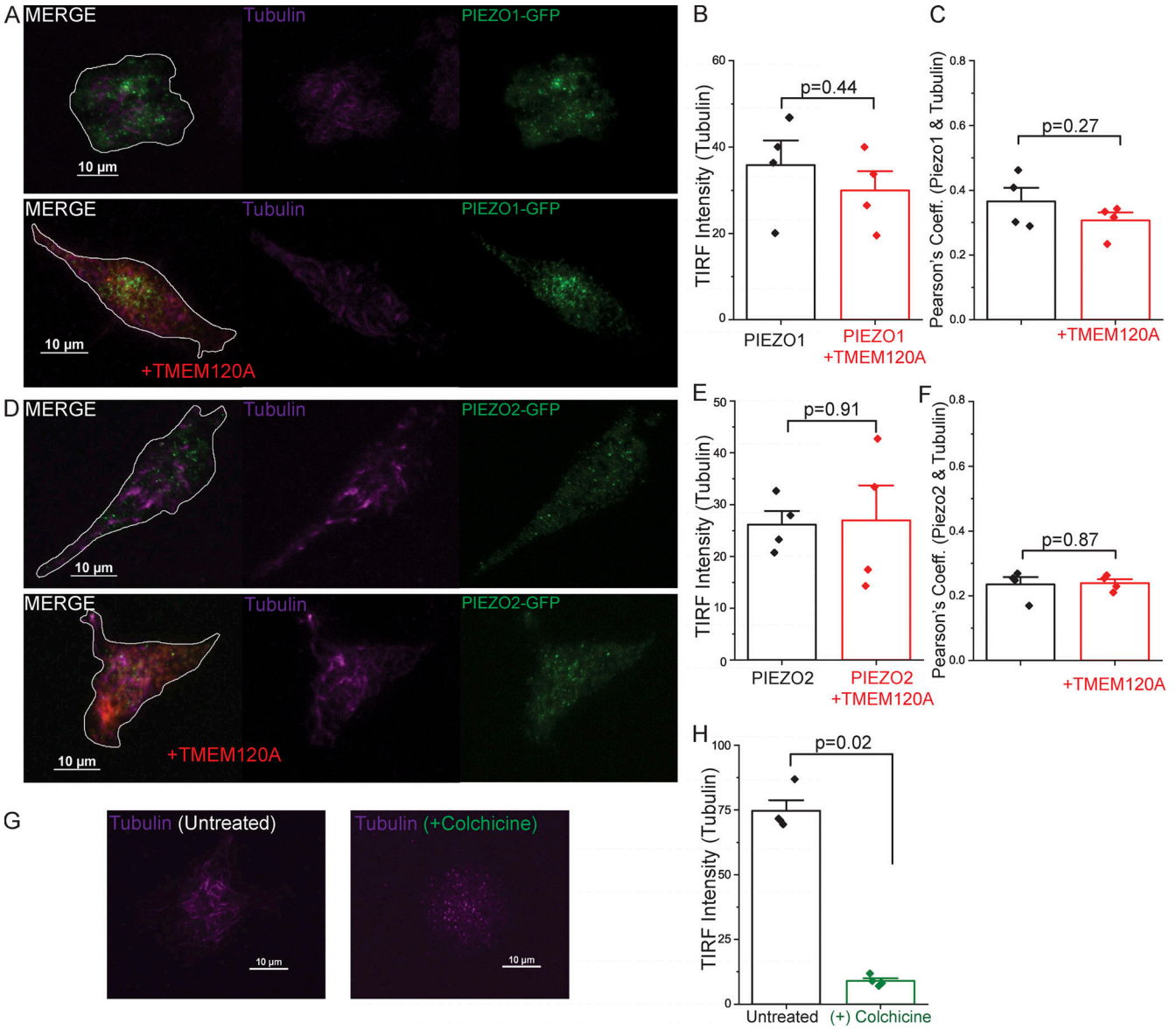

Figure S6. **TMEM120A does not affect the tubulin cytoskeleton.** HEK293 cells were transfected with tdTomato-*Tmem120A* and GFP-*Piezo1* or GFP-*Piezo2*, labeled with Spy650-tubulin, and TIRF images were obtained as described in the Materials and methods section. **(A)** Representative TIRF images for GFP-PIEZO1 and Spy650-tubulin. Cell outlines displayed in white on merged images. **(B)** TIRF intensity of Spy650-tubulin with and without TMEM120A. Statistical significance was calculated using the two-sample *t* test. **(C)** Pearson's coefficient for colocalization of GFP-PIEZO1 and Spy650-tubulin with and without TMEM120A. Statistical significance was calculated using the two-sample *t* test. **(D)** Representative TIRF images for GFP-PIEZO2 and Spy650-tubulin. Cell outlines displayed in white on merged images. **(E)** TIRF intensity of Spy650-tubulin. Statistical significance was calculated using the Welch's *t* test. **(F)** Pearson's coefficient for colocalization of GFP-PIEZO2 and Spy650-tubulin with and without TMEM120A. Statistical significance was calculated using the two-sample *t* test. **(G)** Representative TIRF images for Spy650-tubulin in untreated and colchicine treated cells. **(H)** TIRF intensity of Spy650-tubulin with and without colchicine treatment. Statistical significance was calculated with the Mann-Whitney test. Bar graphs show mean ± SEM and scatter plots. Individual symbols show the average value of cells for one coverslip (5–22 cells/coverslip) from two independent transfections.

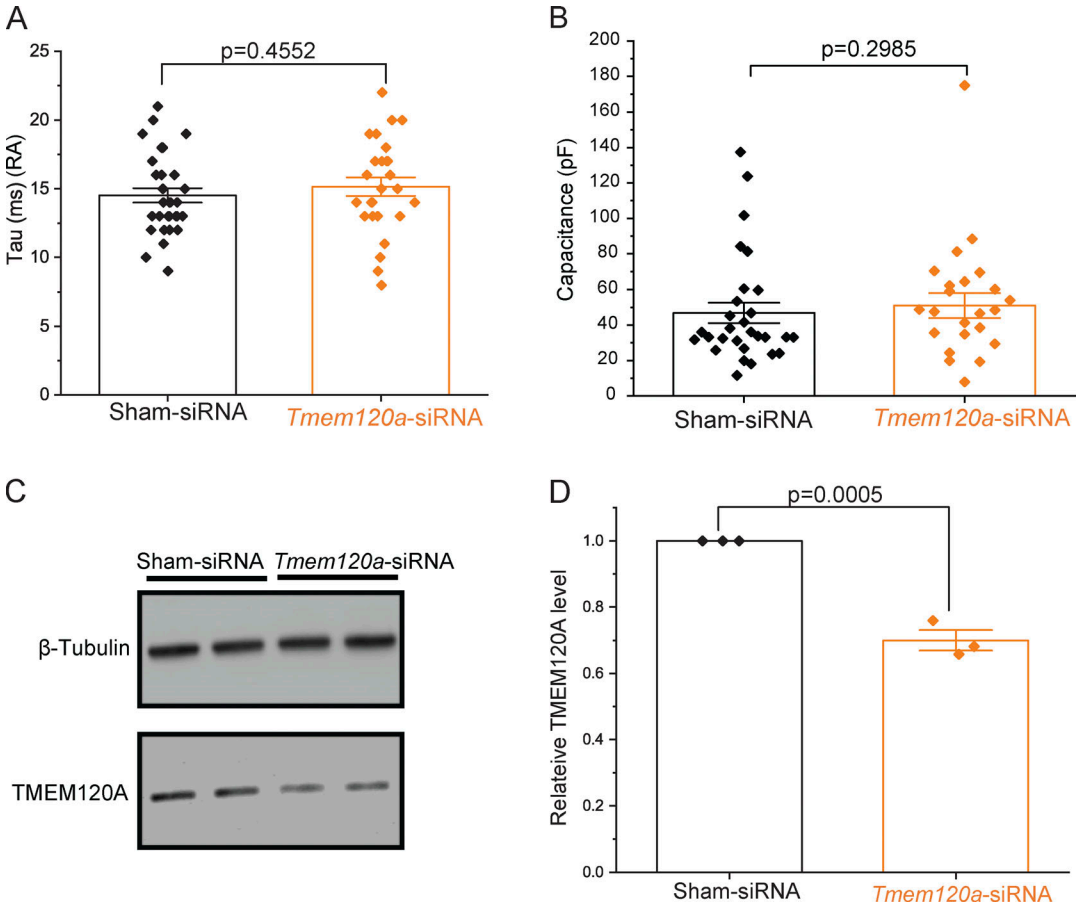

Figure S7. **TMEM120A negatively regulates rapidly adapting mechanically activated currents in mouse DRG neurons.** Data from Fig. 4 showing further analysis of *Tmem120a*-siRNA in mouse DRG neurons and knockdown confirmation in N2A cells. **(A)** Scatter plots and mean ± SEM for the inactivation time constant (tau) for rapidly adapting (RA) currents. Statistical significance was calculated with two-sample *t* test. **(B)** Scatter plots and mean ± SEM of capacitance for neurons displaying RA currents. Statistical significance calculated with the Mann-Whitney test. **(C)** *Piezo1* deficient Neuro2A cells were transfected with Sham-siRNA or *Tmem120a*-siRNA for Western blot analysis as described in the methods section. Representative Western blot image with β-tubulin antibody application (top panel) and TMEM120A antibody application (bottom panel). **(D)** The ratio of TMEM120A band intensity to β-tubulin for each Western blot (three independent transfections) was normalized to Sham-siRNA, scatter plots, and mean ± SEM. Statistical significance calculated with two-sample *t* test. Source data are available for this figure: SourceData FS7.